Steady-State Simulation of LCI-Fed Synchronous Motor Drives Through a Computationally Efficient Algebraic Method

Sobhan Mohamadian, Alberto Tessarolo, *Senior Member, IEEE*, Simone Castellan, and Abbas Shoulaie

***Abstract*—Wound-field synchronous motors (WFSMs) fed by load-commutated inverters (LCIs) are widely used for high-power applications in many fields like ship propulsion, oil and gas industry, and pumped-storage hydropower generation. Several design architectures exist for LCI drives, depending on the number of LCIs and their dc-link connection as well as on the number of WFSM phase count. The prediction of LCI drive performance at steady state is important in the design stage, especially in regard to the prediction of the torque pulsations, which can give rise to serious mechanical resonance issues. This paper proposes an algebraic method to simulate the steady-state behavior of LCI drives in all their configurations of practical interest. Compared to conventional dynamic simulation approaches based on differential equation solution, the method is much more computationally efficient and requires a very limited knowledge of system parameters. Its accuracy is experimentally assessed by comparison against measurements taken on a real LCI drive arranged according to various possible schemes. Furthermore, the advantages of the proposed algebraic method over the dynamic simulations are highlighted by comparison against the simulation results on a high-power LCI-fed WFSM drive in MATLAB/Simulink environment.**

***Index Terms*—Algebraic model, load-commutated inverter, switching function, torque pulsations, wound-field synchronous motors.**

I. Introduction

LOAD-COMMUTATED inverters (LCIs) are frequently used to supply medium-voltage wound-field synchronous motors (WFSMs) in high-power drives for many fields of applications such as the oil and gas industry [1]–[3], large ship propulsion [4]–[6], gas turbine starters [7], and pumped-storage hydropower plants [8]. LCI drives are practically used in different possible design arrangements. The simplest one consists of a conventional three-phase WFSM fed by a single LCI [4]; in order to improve the output torque quality and enhance system fault tolerance, a dual three-phase WFSM is also frequently adopted wherein the two-stator three-phase windings are supplied by two LCIs [4], [9]–[11]. Furthermore, to mitigate possible interharmonic issues in the dc-link current and output torque, the two LCIs can have their dc links suitably interconnected [12].

The prediction of LCI drive operation at steady state is important in the system design stage, especially in order to predict the output torque waveform and its harmonic spectrum. In fact, torque harmonics are known to be a possible source for severe mechanical resonance phenomena [2], [12], [13], which need to be carefully avoided in the design stage.

The conventional approach to predict LCI performance is based on modeling the drive system in such dynamic simulation environments as MATLAB/Simulink [14]. This is known to pose some challenges mainly due to the following reasons: the computational burden, especially if many operating conditions have to be investigated [13]; the need to wait for the system to reach a steady-state working point; an appropriate setting of initial conditions [15]; the accurate knowledge of system parameters, in particular those included in the WFSM dynamic model [16]; and the knowledge of PI regulator parameters of control loops.

In this paper, a method is proposed to simulate the steady-state performance of LCI drives, making use of appropriate switching functions [17]–[19]. The approach is very flexible as it can be easily adapted to fit all the aforementioned LCI drive arrangements of practical interest. Compared to conventional dynamic simulations, as it will be shown in Section VI, it brings the following advantages: it does not involve the solution of any differential equation and only includes closed-form algebraic formulas, resulting in a fairly higher computational efficiency and much faster simulation times; it does not require initial condition setting; it does not need to wait for steady-state conditions to be reached; it requires a limited set of system parameters. A restraint of the method is that it works only for steady-state operation and is not suitable for investigating drive operation during transients.

The methodology is experimentally assessed against measurements taken on a real drive system configured according to different design schemes. In all the arrangements and working conditions taken into account, the proposed approach is shown to yield accurate results, which are in satisfactory accordance with measurements.

The paper is organized as follows. In Section II, the main drive configurations under study and the prototype drive used for validations are described; in Section III, an algebraic model is derived to determine dc-link voltages; in Section IV, dc-link voltages are used to compute dc-link currents; in Section V,

Manuscript accepted January 13, 2016.

S. Mohamadian and A. Shoulaie are with the Department of Electrical Engineering, Iran University of Science and Technology, 1684613114 Tehran, Iran (e-mail: s_mohamadian@iust.ac.ir; shoulaie@iust.ac.ir).

A. Tessarolo and S. Castellan are with the Department of Engineering and Architecture, University of Trieste, 34127 Trieste, Italy (e-mail: atessarolo@units.it; scastellan@units.it).

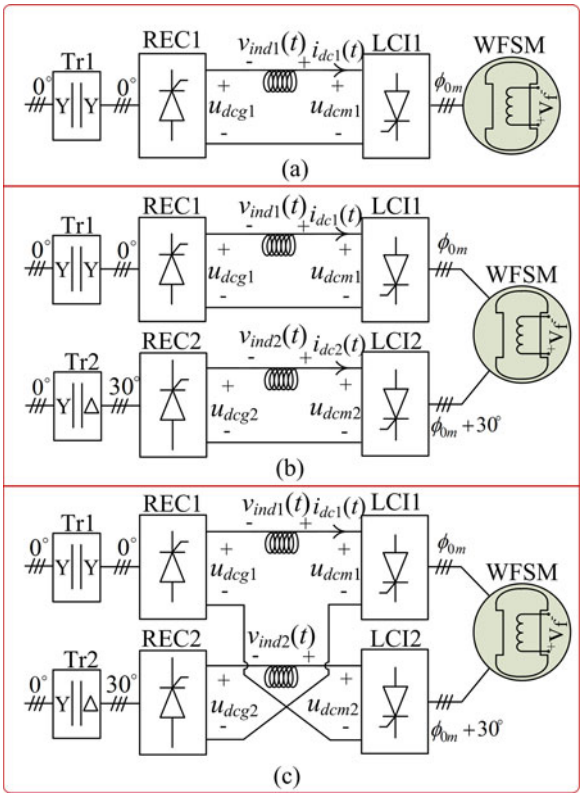

Fig. 1. Possible LCI-fed drive system arrangements: (a) single three-phase LCI-fed WFSM; (b) dual three-phase LCI-fed WFSM with independent converters; (c) dual three-phase LCI-fed WFSM with interconnected dc links.

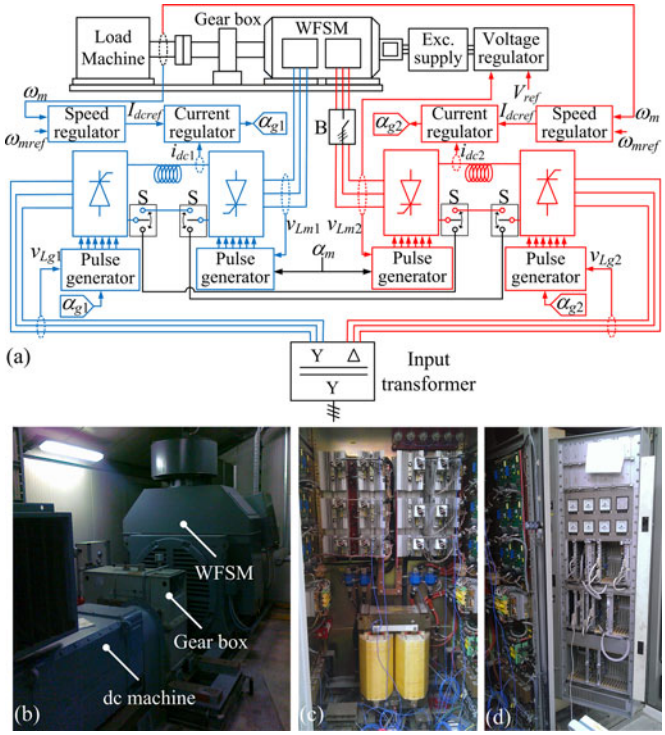

Fig. 2. (a) Block scheme of the experimental equipment (single three-phase LCI-fed WFSM if switch *B* is open and switches *S* are in the upper position, dual-three-phase LCI-fed WFSM with independent converters if switch *B* is closed and switches *S* are in the upper position, dual three-phase LCI-fed WFSM with interconnected dc links if switch *B* is closed and switches *S* are in the lower position); (b) dual three-phase machine used as the LCI-fed motor and dc generator used as the load; (c) converter and input transformer cubicle; and (d) control cubicle.

both dc-link voltages and currents are used to derive an algebraic algorithm to obtain motor torque waveform. In each of the aforementioned sections, the description of the calculation procedure is followed by its relevant experimental validation. Finally, in Section VI, MATLAB simulations are provided to better highlight the advantages of the proposed method over conventional dynamic simulation approaches.

II. Possible LCI Drive Topologies and Their Modeling Approach

A. Description of the Topologies

In Fig. 1, the three dominant types of LCI-fed drives are depicted. Single three-phase LCI-fed drives [see Fig. 1(a)] are widely used in grid-connected gas turbine starters [7] and pumped-storage hydropower plants [8]. In order to mitigate the dominant torque harmonic component (having six times the motor supply frequency, [14]) in a single three-phase drive, dual three-phase WFSMs are employed in most high-power, medium-voltage industrial drives where two separate three-phase LCIs feed the electric motor, as shown in Fig. 1(b). However, some interharmonics can arise in the dc-link current due to the difference between motor and mains frequencies [12]. These interharmonic currents contribute to torque pulsations, which can cause catastrophic mechanical resonances if their frequency is near to one torsional natural frequency (TNF) of the overall plant shaft line [13]. In the attempt to prevent the problem, dual three-phase LCI-fed drives with interconnected dc links [see Fig. 1(c)] are proposed [12].

The mentioned LCI drive topologies will be investigated in this paper by proposing a computationally efficient approach to predict their steady-state performance with no need for dynamic simulations. The proposed approach will be assessed using the experimental setup, shown in Fig. 2, which can be arranged in the three configurations, shown in Fig. 1, by suitably setting switches *S* and *B*, as explained in Fig. 2. As it can be seen from Fig. 2, there are mainly three control loops, used to, respectively, control the following quantities: speed, dc-link current, and field current. Three reference values are set off-line to the desired values (test conditions are mentioned in Table IV) by the operator, namely, the reference speed, the firing angle of the LCIs, and the reference stator line-to-line rms voltage. The latter is used to control the field current so that the stator line-to-line rms voltage follows the reference value through a PI regulator. This PI regulator outputs the firing angle of a phase-controlled rectifier, which feeds the rotor excitation circuit. A dc motor is coupled to the WFSM shaft acting as a generator (load for the WFSM) injecting the power back to the grid via a phase-controlled converter. The measured data are sampled with a sampling frequency of 100 kHz (apart from the torque, for which the sampling frequency is 10 kHz), saved in Excel formats, and then processed by MATHCAD software.

TABLE I
WFSM RATINGS

Power	250 kW	Power factor	0.9
Line-to-line voltage	380 V	Speed	1500 r/min
Stator phase current	225 A	Number of poles	4

TABLE II
DC-LINK INDUCTANCE AND WFSM PARAMETERS USED IN THE ANALYTICAL MODEL

L_{dc}	3.8 mH	L''_d	0.25 mH
R_s	0.0043 Ω	L''_q	0.27 mH

TABLE III
ADDITIONAL PARAMETERS OF THE EXPERIMENTAL WFSM

d-Axis transient open-circuit time constant T'_{d0}	3.5 s	*d*-Axis transient short-circuit time constant T'_d	0.22 s
d-Axis subtransient short-circuit time constant T''_d	0.009 s	Unsaturated direct synchronous reactance X_d	9.0 mH
d-Axis transient reactance X'_d	0.48 mH	*q*-Axis synchronous reactance X_q	2.9 mH
Negative sequence reactance X_2	0.26 mH	Motor mass	1800 kg
Zero-sequence reactance X_0	0.14 mH	Moment of inertia *J*	10.4 kg·m^2

TABLE IV
WORKING POINTS OF THE RECORDED WAVEFORMS FOR THE LCI-FED DRIVE TOPOLOGIES

	Single-Three-Phase Drive	Dual-Three-Phase Drive with Separate DC Links	Dual three-phase Drive with Interconnected DC Links
Motor speed [r/min] ω_m	1484	1490	1220
LCI firing angle (°) α_m	140	150	150
Line-to-line voltage (V) $V_{L\,r\,m\,s}$	374	374	340
DC-Link Current (A) I_{dc}	108	52	56

Machine ratings and parameters needed for the analytical approach are reported in Tables I and II, respectively. It can be noted that only a very limited number of parameters is needed, namely, the dc-link inductance L_{dc}, stator phase resistance R_s, and the subtransient *d*- and *q*-axes inductances L''_d and L''_q. In addition to the data listed in Tables I and II, some more parameters of the machine are available in Table III.

B. Algebraic Modeling Approach

For some types of studies, the transient behavior of the drive can be of interest; in this case, its complete dynamic modeling in such environments as MATLAB/Simulink is necessary, as discussed in [14]. In many other circumstances, the designer can be interested in predicting only the steady-state performance of the drive. In this case, running numerical dynamic simulation, based on solving a system of highly nonlinear differential equations, which model the machine, the power electronics, and the control algorithms, can be redundant and a computationally efficient approach can be adopted, as proposed next, based on purely algebraic analytical calculations. The methodology is mainly aimed at analytically predicting the waveforms of the following quantities: the dc-link voltage, the dc-link current, and the electromagnetic torque for all the drive configurations presented in Section II-A. The torque waveform is the quantity of highest practical interest due to the well-known potentially adverse impact of its harmonic components. However, the dc-link voltages and current waveforms can be computed first as their knowledge is required for torque waveform prediction.

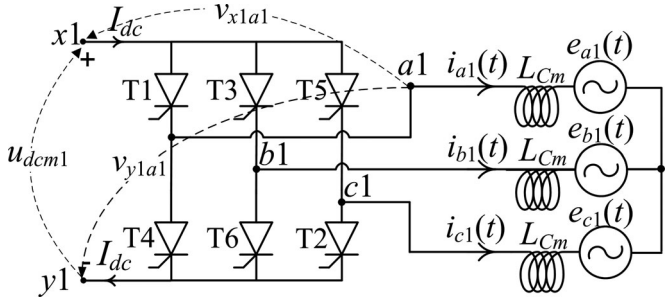

Fig. 3. Simplified equivalent circuit of the first three-phase winding set of the dual three-phase WFSM connected to LCI1.

Different parameters, such as the firing angle of the LCIs and rectifiers, the commutation inductance, the different frequencies of the grid- and motor-side ac voltages, the different possible types of dc-link connections (see Fig. 1), the voltage amplitudes on the ac sides and the dc-link inductance, can affect the torque waveform. As it will be clarified later by analyzing the harmonic spectrum of the dc-link voltage, current, and torque, the effect of all the aforementioned parameters can be studied by the use of the proposed analytical model.

III. DC-LINK VOLTAGE PREDICTION

DC-link voltages are not very significant quantities in themselves; however, they need to be estimated as a basic data for the subsequent evaluation of dc currents and motor torque waveforms.

DC-link voltages either at the rectifier's outputs (u_{dcg1} or u_{dcg2}) or LCI's inputs (u_{dcm1} or u_{dcm2}) are independent of the dc-links type of connection (see Fig. 1). Each of these voltages can be extracted by analyzing the ac-side voltages of each converter (on both motor and grid sides) through properly defined switching functions, which are determined by the conduction sequences of its thyristors. The approach to calculate the dc-link voltage is next explained in detail for LCI1, i.e., with respect to u_{dcm1}, as the other dc-link voltages can be computed with exactly the same procedure applied to the other thyristor bridges.

A. Model Description

For the purpose of computing u_{dcm1}, the equivalent circuit shown in Fig. 3 is used. Fig. 3 shows LCI1 connected to a

three-phase winding set of the WFSM. In this model, the stator phase resistances of the motor are neglected [20] and each motor phase is modeled as a sinusoidal back electromotive force (EMF) in series with the commutating inductance, L_{Cm} [20]. In regard to the motor phase back EMF, its actual waveform is slightly distorted due to the rotor saliency, which mainly causes the third, fifth, and seventh harmonics to arise in it. However, the rotor pole shoe is typically shaped so that the total harmonic distortion of the no-load voltage is less than 2% and the amplitude of each harmonic component is usually less than 1% of the fundamental [21]. This makes it definitely reasonable to model the motor back EMF with a sinusoidal wave. Since the motor back-EMF waveform is also a function of rotor speed, it could be affected by speed pulsations due to the torque ripple. However, in high-power machines (fed by LCI drives), the rotor moment of inertia is such that torque pulsations have no significant effect on the speed. This is confirmed by the fact that, both based on measurements and on simulations, speed oscillations are lower than 1% at steady-state and rated conditions.

The voltage $e_{a1}(t)$ represents the back EMF across phase *a* of the first three-phase winding set, and, being assumed to have a sinusoidal waveform, it can be written as

$$e_{a1}(t) = V_m \sin(\omega_m t - \phi_{0m}) \tag{1}$$

where the subscript *m* refers to motor-side quantities, ω_m is the motor electrical pulsation in rad/s, V_m is the amplitude of the phase voltages, and ϕ_{0m} is the initial phase angle. The other phase voltages are properly displaced, i.e., by either $+120$ or -120 electrical degrees, with respect to phase "*a*1."

Disregarding the dc-link current ripple, L_{Cm} acts only during the commutation intervals, i.e., when the current path changes from one phase to the other. For high-power synchronous machines, L_{Cm} can be sufficiently approximated as a time-invariant quantity equal to the average of the *d*-axis and *q*-axis subtransient inductances, i.e., $\left(L''_d + L''_q\right)/2$ [20].

It should be mentioned that the impact of a commutation occurring in one LCI, e.g., LCI2, on the dc-link voltage of the other LCI, e.g., u_{dcm1} in Fig. 1, is negligible. This fact is explained in Appendix A and justifies the fact that the voltage at each converter dc terminals can be determined disregarding the other converters.

More precisely, the dc-link voltage of each individual LCI is going to be computed as the sum of two terms: the no-load dc-link voltage u^0_{dcm1}, which would appear in the absence of currents (i.e., disregarding the commutation voltage drops), plus the commutation voltage drop $\Delta u^L_{\mathrm{dcm1}}$ across L_{Cm}. In other words, we can write

$$u_{\mathrm{dcm1}}(t) = u^0_{\mathrm{dcm1}}(t) + \Delta u^L_{\mathrm{dcm1}}(t). \tag{2}$$

Consistently with (2), superscript "0" will be used in the paper to denote voltages disregarding commutation phenomenon, while superscript "L" will denote the correction terms to be added to these voltages in order to account for commutations.

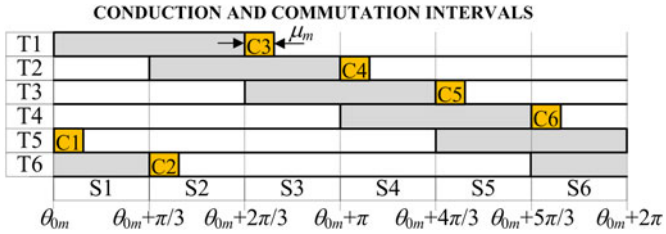

Fig. 4. Switching scheme of the thyristors in LCI1.

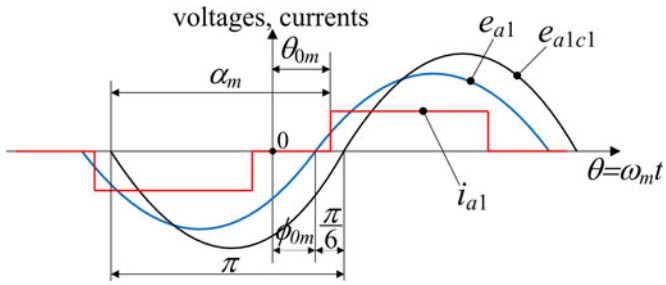

Fig. 5. Schematic waveforms for currents i_{a1} and voltages e_{a1}, e_{a1c1}.

B. Expression of the DC-Link Voltage as a Function of AC-Side Voltages

The algebraic computation of dc-link voltages requires the use of appropriately defined switching functions, which are meant to transfer the thyristor switching or commutation patterns into closed-form mathematical expressions.

The basic idea of the switching functions used in this paper is that the dc-side voltages in each thyristor converter bridge can be univocally determined once the switching sequence is defined. By switching sequence, we mean a diagram like the one shown in Fig. 4 for LCI1. In this scheme, there are two types of conduction intervals: 1) normal conduction intervals, lasting 120 electrical degrees each, where two thyristors belonging to different phases conduct simultaneously; 2) commutation intervals, which are characterized by the simultaneous conduction of three thyristors, with a duration of μ_m electrical degrees each (μ_m being the commutation overlap angle [10]). θ_{0m} in Fig. 4 is equal to $\phi_{0m} - \pi + \pi/6 + \alpha_m$, with α_m being the firing angle of T1 measured with respect to its reference, selected as the zero-crossing instant at which the voltage $e_{a1c1}(t)$ changes from positive to negative. This is graphically illustrated in Fig. 5. Regarding the terminal motor-side and line-side voltages, these are assumed to be sinusoidal only for illustration purposes, i.e., to show the phase relationships among them and between them and the currents. In the calculations, the commutation voltage drops occurring in line-side and motor-side voltages are fully accounted for. Also, the dc-link current is assumed to be smooth in the computation of the dc-link voltage. Neglecting current ripples is not an issue in computing the commutation drops because commutations are very short. Instead, the assumption of smooth dc-link current introduces some differences between analytical and experimental dc-link voltages. Later, the effect

of this approximation and the various sources of discrepancies between the measured and reconstructed dc-link voltages will be discussed in more detail.

In order to compute u_{dcm1} with a switching function approach it is convenient to express u_{dcm1} as (see Fig. 3)

$$\begin{aligned} u_{\mathrm{dcm1}}(t) &= v_{x1a1}(t) - v_{y1a1}(t) \\ &= \left[v^0_{x1a1}(t) + \Delta v^L_{x1a1}(t)\right] - \left[v^0_{y1a1}(t) + \Delta v^L_{y1a1}(t)\right] \\ &= u^0_{\mathrm{dcm1}}(t) + \Delta u^L_{\mathrm{dcm1}}(t) \end{aligned} \tag{3}$$

where $v_{x1a1}(t)$ is the voltage $v_{x1}(t) - v_{a1}(t)$ between points $x1$ and $a1$; $v_{y1a1}(t)$ is the voltage $v_{y1}(t) - v_{a1}(t)$ between points $y1$ and $a1$; superscripts "0" and "L" denote, as usual, the quantities computed disregarding commutation voltage drops and the correction terms to account for the latter; $u^0_{\mathrm{dcm1}}(t) = v^0_{x1a1}(t) - v^0_{y1a1}(t)$ and $\Delta u^L_{\mathrm{dcm1}}(t) = \Delta v^L_{x1a1}(t) - \Delta v^L_{y1a1}(t)$.

On the other side, the voltages between a phase terminal and points $x1$ and $y1$ disregarding commutations [e.g., $v^0_{x1a1}(t)$ and $v^0_{y1a1}(t)$ appearing in (3)] are shifted by 180 electrical degrees with respect to each other with reverse polarity, i.e., $v^0_{y1a1}(t) = -v^0_{x1a1}(t + \pi/\omega_m)$. For example, let us take an instant $t = t_0$ at which T3 and T2 are conducting (interval S3 in Fig. 4) so that the point $x1$ is connected to $b1$ in Fig. 3 and $v^0_{x1a1}(t)$ is equal to $-e_{a1}(t_0) + e_{b1}(t_0)$ because the current is assumed to be smooth and its consequent voltage drop across L_{Cm} is zero. At $t = t_0 + \pi/\omega_m$, T6 and T5 are conducting (interval S6 in Fig. 4) so that point $y1$ is connected to point $b1$ in Fig. 3 and $v^0_{y1a1}(t)$ is equal to $-e_{a1}(t_0 + \pi/\omega_m) + e_{b1}(t_0 + \pi/\omega_m)$, which, being e_{a1} and e_{b1} sinusoidal, is equal to $-v^0_{x1a1}(t_0)$. This holds for any choice of t_0 and thereby proves that

$$v^0_{y1a1}(t) = -v^0_{x1a1}(t + \pi/\omega_m). \tag{4}$$

As a consequence, we can write

$$u^0_{\mathrm{dcm1}}(t) = v^0_{x1a1}(t) - v^0_{y1a1}(t) = v^0_{x1a1}(t) + v^0_{x1a1}(t + \pi/\omega_m). \tag{5}$$

Similarly, the term $\Delta u^L_{\mathrm{dcm1}}(t)$ can be defined as a function of the voltage drops between phase $a1$ terminal and points $x1$ and $y1$ during commutation periods, i.e., $\Delta v^L_{x1a1}(t)$ and $\Delta v^L_{y1a1}(t)$, as

$$\begin{aligned} \Delta u^L_{\mathrm{dcm1}}(t) &= \Delta v^L_{x1a1}(t) - \Delta v^L_{y1a1}(t) \\ &= \Delta v^L_{x1a1}(t) + \Delta v^L_{x1a1}(t + \pi/\omega_m) \end{aligned} \tag{6}$$

where the equality $\Delta v^L_{y1a1}(t) = -\Delta v^L_{x1a1}(t + \pi/\omega_m)$ is explained in Appendix B.

In conclusion, (2) can be rewritten according to (5) and (6) as

$$\begin{aligned} u_{\mathrm{dcm1}}(t) &= \left[v^0_{x1a1}(t) + v^0_{x1a1}(t + \pi/\omega_m)\right] \\ &\quad + \left[\Delta v^L_{x1a1}(t) + \Delta v^L_{x1a1}(t + \pi/\omega_m)\right]. \end{aligned} \tag{7}$$

C. Algebraic Calculation of DC-Link Voltages Through Switching Function Approach

Equation (7) proves that the dc-link voltage is fully determined provided that the ac-side voltage functions $v^0_{x1a1}(t)$ and $\Delta v^L_{x1a1}(t)$ are known. In the next two sections, the procedure to compute such terms through appropriate switching functions will be explained.

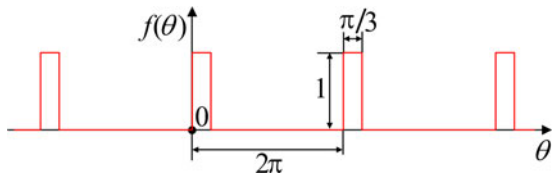

Fig. 6. Periodic function $f(\theta)$.

1) Computation of $v^0_{x1a1}(t)$: In order to define $v^0_{x1a1}(t)$ algebraically with a switching function approach, some insight into the detailed operation of the converter LCI1 is needed. The converter operation will be analyzed in all the conduction intervals S1, S2, ..., S6, shown in Fig. 4, by disregarding commutations [i.e., intervals C1, C2, ..., C6, which will be taken into account when dealing with $\Delta v^L_{x1a1}(t)$].

In the first and second intervals (S1 and S2) of the switching scheme shown in Fig. 4, T1 is in the conduction path and $v^0_{x1a1}(t)$ is equal to zero for $\theta_{0m} < \theta < \theta_{0m} + 2\pi/3$. During S3 and S4, T3 is conducting and $v^0_{x1a1}(t)$ is simply equal to $-e_{a1}(t) + e_{b1}(t)$. Therefore, for $\theta\theta_{0m} + 2\pi/3 < q < \theta_{0m} + 4\pi/3$, $v^0_{x1a1}(t)$ is equal to

$$v^0_{x1a1}(t) = \begin{bmatrix} -1 & 0 & 0 \end{bmatrix} \mathbf{v}_{m1}(t) \tag{8}$$

where

$$\mathbf{v}_{m1}(t) = \begin{pmatrix} e_{a1}(t) - e_{b1}(t) \\ e_{b1}(t) - e_{c1}(t) \\ e_{c1}(t) - e_{a1}(t) \end{pmatrix}. \tag{9}$$

Similarly, during S5 and S6 ($\theta_{0m} + 4\pi/3 < \theta < \theta_{0m} + 2\pi$), T5 is conducting and $v^0_{x1a1}(t)$ is equal to $-e_{a1}(t) + e_{c1}(t)$. Thus

$$v^0_{x1a1}(t) = \begin{bmatrix} 0 & 0 & 1 \end{bmatrix} \mathbf{v}_{m1}(t). \tag{10}$$

Consequently, if we define the 6×3 matrix

$$\mathbf{S}_0 = \begin{pmatrix} 0 & 0 & 0 \\ 0 & 0 & 0 \\ -1 & 0 & 0 \\ -1 & 0 & 0 \\ 0 & 0 & 1 \\ 0 & 0 & 1 \end{pmatrix} \tag{11}$$

then $v^0_{x1a1}(t)$ can be written in a compact matrix form as follows:

$$v^0_{x1a1}(t) = \sum_{j_m=1}^{6} \left[\mathbf{S}_0 \;\; \mathbf{v}_{m1}(t)\right]_{j_m} f\left(\omega_m t - \theta_{0m} + \tfrac{\pi}{3} - j_m \tfrac{\pi}{3}\right) \tag{12}$$

where $[\bullet]_{j_m}$ indicates the j_mth element of the vector in square brackets and $f(\theta)$ is the function plotted in Fig. 6, which can be

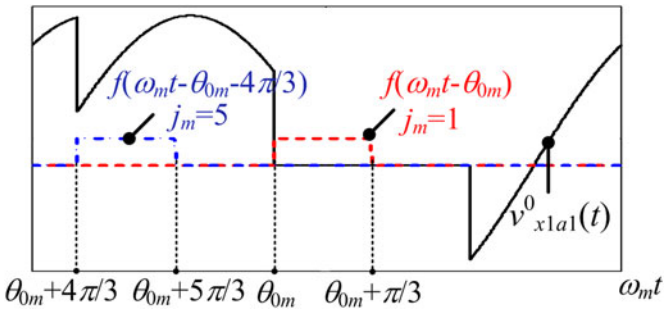

Fig. 7. $v^0_{x1a1}(t)$ and $f(\omega_m t-\theta_{0m}-(j_m-1)\pi/3)$ for $j_m=5$ and $j_m=1$ in a period of motor frequency.

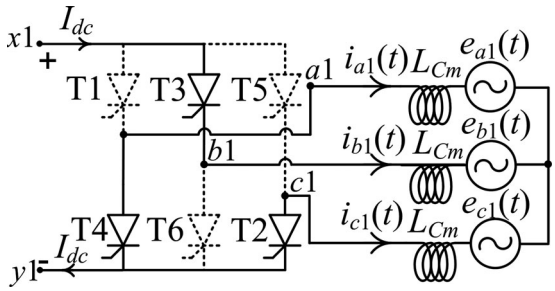

Fig. 8. Equivalent circuit during the commutation interval C4 in LCI1 (conduction paths are shown in solid lines).

defined with the following analytical expression:

$$f(\theta)=\begin{cases}1, & \text{if } 0\le \mathrm{mod}\left(|\theta|-\dfrac{\pi}{6}\left[\mathrm{sgn}(\theta)-1\right],2\pi\right)<\dfrac{\pi}{3}\\ 0, & \text{otherwise}\end{cases}. \tag{13}$$

In (13), mod(*a,b*) returns the remainder on dividing a by b and sgn(θ) is equal to 1 if θ is zero or positive, to -1 if θ is negative.

As an illustration $v^0_{x1a1}(t)$ is plotted in Fig. 7 for a typical operating point. Disregarding the scales of the vertical axis, the function $f(\omega_m t-\theta_{0m}-(j_m-1)\pi/3)$ is also plotted for $j_m=5$ and $j_m=1$. According to (12), v^0_{x1a1}, at any time, is equal to the sum of all the elements of a 61 vector. However, depending on the time instant and because of the function $f(\theta)$ defined in (13), all the elements are zero except one. For instance, for $\theta_{0m}+4\pi/3<\omega_m t<\theta_{0m}+5\pi/3$ (the fifth interval, S5, in Fig. 4), $f(\omega_m t-\theta_{0m}-(j_m-1)\pi/3)$ in (12) is only nonzero for $j_m=5$, as shown in Fig. 7, and $v^0_{x1a1}(t)$ is consequently equal to the fifth element of the vector $[\mathbf{S}_0\ \mathbf{v}_{\mathrm{m}1}(t)]$ as also computed in (10).

2) Computation of $\Delta v^L_{x1a1}(t)$*:* Due to the inductance L_{Cm} shown in Fig. 3, the current commutation between two subsequent conducting thyristors is not instantaneous and lasts for a time interval equal to μ_m/ω_m, where μ_m is the commutation overlap angle. The commutation intervals for LCI1 are denoted in Fig. 4 as *Ck* with $k=1,2,\ldots,6$. Neglecting the stator phase resistance, the commutation angle μ_m is calculated with the following equation [20]:

$$\mu_m=\arccos\left[\alpha_m-\frac{2L_{Cm}\omega_m I_{\mathrm{dc}}}{V_m\sqrt{3}}\right]. \tag{14}$$

During C1 $(\theta_{0m}<\theta<\theta_{0m}+\mu_m)$, $e_{a1c1}(t)$ drives the current in phase $a1$ to increase from 0 to I_{dc} and to decrease in the opposite direction in phase $c1$. Therefore, phases $a1$ and $c1$ are short circuited and both switches T1 and T5 in addition to T6 are conducting. In C2 $(\theta_{0m}+\pi/3<\theta<\theta_{0m}+\pi/3+\mu_m)$, T2 and T6 are, respectively, the incoming and the outgoing thyristors, which conduct simultaneously together with T1. Thus, during the first two commutation intervals (C1 and C2), T1 is on and the commutation between (T1, T5) and (T6, T2) does not affect $v_{x1a1}(t)$, which remains equal to zero like $v^0_{x1a1}(t)$ during S1 and S2. In other words, $\Delta v^L_{x1a1}(t)$ is equal to zero in C1 and C2.

During C3 $(\theta_{0m}+2\pi/3<\theta<\theta_{0m}+2\pi/3+\mu_m)$, T1 and T3 are conducting simultaneously and $v_{x1a1}(t)$ is still zero. Since $v^0_{x1a1}(t)$ is equal to $(-e_{a1}(t)+e_{b1}(t))$ during S3, the difference from the case without commutation, i.e., $\Delta v^L_{x1a1}(t)=v_{x1a1}(t)-v^0_{x1a1}(t)$, during C3 is equal to $-(-e_{a1}(t)+e_{b1}(t))$. In other words, for C3, we can write

$$\Delta v^L_{x1a1}(t)=\begin{bmatrix}1 & 0 & 0\end{bmatrix}\mathbf{v}_{m1}(t) \tag{15}$$

During C4 $(\theta_{0m}+\pi<\theta<\theta_{0m}+\pi+\mu_m)$, the commutation between T2 and T4 occurs while T3 is also conducting. By applying Kirchhoff voltage law to the short-circuit loop shown in Fig. 8, one can write

$$L_{Cm}\frac{di_{a1}}{dt}+e_{a1}(t)=L_{Cm}\frac{di_{c1}}{dt}+e_{c1}(t). \tag{16}$$

As $i_{a1}(t)+i_{c1}(t)=-I_{\mathrm{dc}}$ is constant under the hypothesis of disregarding the dc-link current ripple, we obtain

$$\frac{di_{a1}}{dt}=\frac{-di_{c1}}{dt}. \tag{17}$$

Substituting (17) into (16) yields

$$\frac{di_{a1}}{dt}=\frac{e_{c1}(t)-e_{a1}(t)}{2L_{Cm}}. \tag{18}$$

Also, the expression for $v_{x1a1}(t)$ is extracted from Fig. 8 by applying Kirchhoff voltage law to the path, including $x1$, T3, $e_{b1}(t)$, $e_{a1}(t)$, and $a1$ yielding

$$v_{x1a1}(t)=-e_{a1}(t)+e_{b1}(t)-L_{Cm}\frac{di_{a1}}{dt} \tag{19}$$

where it has been taken into account that the current in phase "$b1$" is constant and does produce no voltage drop across L_{Cm}. Substituting (18) into (19) gives

$$v_{x1a1}(t)=e_{b1}(t)-\frac{e_{a1}(t)+e_{c1}(t)}{2}. \tag{20}$$

According to (20) and considering that, as per (8), $v^0_{x1a1}(t)$ is equal to $-e_{a1}(t)+e_{b1}(t)$ during S4, we can conclude that $\Delta v^L_{x1a1}(t)$ during C4 is

$$\Delta v^L_{x1a1}(t)=v_{x1a1}(t)-v^0_{x1a1}(t)=\frac{e_{a1}(t)-e_{c1}(t)}{2}. \tag{21}$$

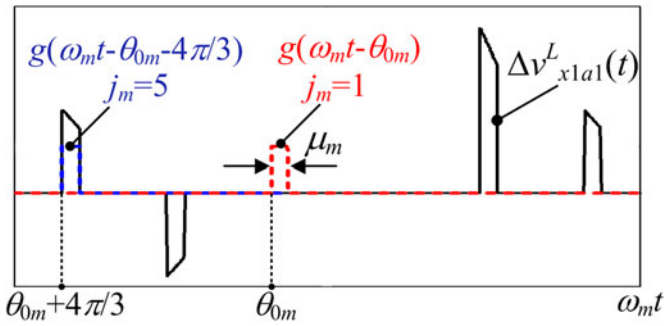

Fig. 9. $\Delta v_{x1a1}^{L}\ (t)$ and $g\left(\omega_m t-\theta_{0m}-\left(j_m-1\right)\pi/3\right)$ for $j_m=5$ and $j_m=1$ in a period of motor frequency.

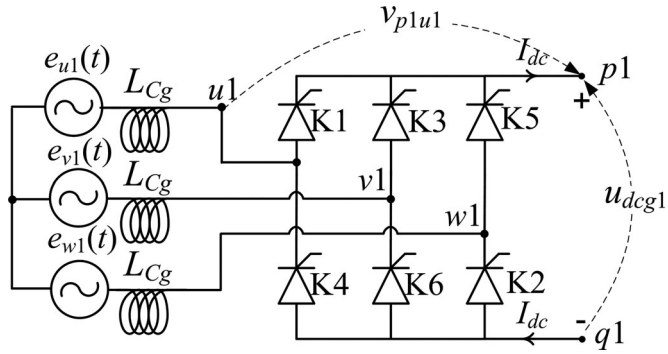

Fig. 10. Circuit diagram of REC1 with its corresponding grid three-phase voltages and commutation inductances L_{cg}.

The same approach as for C4 can be followed to extract $\Delta v_{x1a1}^{L}(t)$ during the fifth and sixth commutation intervals (C5 and C6). The final expressions for these two intervals are shown in (22) and (23), respectively

$$\Delta v_{x1a1}^{L}(t)=\frac{e_{b1}(t)-e_{c1}(t)}{2},\quad \text{for } \theta_{0m}+\frac{4\pi}{3}<\theta<\theta_{0m}+\frac{4\pi}{3}+\mu \tag{22}$$

$$\Delta v_{x1a1}^{L}(t)=\frac{e_{a1}(t)-e_{b1}(t)}{2},\quad \text{for } \theta_{0m}+\frac{5\pi}{3}<\theta<\theta_{0m}+\frac{5\pi}{3}+\mu. \tag{23}$$

In conclusion, all the expressions found for $\Delta v_{x1a1}^{L}(t)$ in the commutation intervals C1.C6 can be combined into the single compact matrix form shown below

$$\Delta v_{x1a1}^{L}(t)=\sum_{j_m=1}^{6}\left[\mathbf{S}_L\ \mathbf{v}_{m1}(t)\right]_{j_m}\ g\left(\omega_m t-\theta_{0m}+\frac{\pi}{3}-j_m\frac{\pi}{3}\right) \tag{24}$$

where

$$\mathbf{S}_L=\frac{1}{2}\begin{pmatrix}0&0&0\\0&0&0\\2&0&0\\0&0&-1\\0&1&0\\1&0&0\end{pmatrix} \tag{25}$$

and

$$g(\theta)=\begin{cases}1, & \text{if } 0\le \operatorname{mod}\left(|\theta|-\dfrac{\mu_m}{2}\left[\operatorname{sgn}(\theta)-1\right],2\pi\right)<\mu_m\\ 0, & \text{otherwise}\end{cases}. \tag{26}$$

The function $g(\theta)$ has the same waveform as $f(\theta)$ shown in Fig. 6 except for its "pulse" duration, which is not $\pi/3$ but μ_m.

As an illustration $\Delta v^{Lx1a1}(t)$ is plotted in Fig. 9 for a typical operating point. Disregarding the scales of the vertical axis, the function $g\left(\omega_m t-\theta_{0m}-\left(j_m-1\right)\pi/3\right)$ is also plotted for $j_m=5$ and $j_m=1$. According to (24), Δv_{x1a1}^{L} at each time instant is equal to the sum of all the elements of a 61 vector. However, during each commutation period, all the elements are zero except one. For instance, for $\theta_{0m}+4\pi/3<\omega_m t<\theta_{0m}+4\pi/3+\mu_m$ (the fifth commutation interval, C5, in Fig. 4), $g\left(\omega_m t-\theta_{0m}-\left(j_m-1\right)\pi/3\right)$ in (26) is only nonzero for $j_m=5$, as shown in Fig. 9, and Δv_{x1a1}^{L} is consequently equal to the fifth element of the vector $[\mathbf{S}_{\mathrm{L}}\ \mathbf{v}_{\mathrm{m}1}(t)]$ as also computed in (22).

3) Note on the Computation of $u_{\mathrm{dcm2}}(t)$, $u_{\mathrm{dcg1}}(t)$, $u_{\mathrm{dcg2}}(t)$*:* Up to this point, the detailed procedure for the computation of the dc-link voltage $u_{\mathrm{dcm1}}(t)$ of LCI1 through an algebraic switching-function approach has been explained. As mentioned before, the other bridges of the drive can be treated in the same manner by considering that their switching sequence and their ac-side voltages are properly displaced with respect to the case of LCI1.

In particular, the grid-side dc-link voltage u_{dcg1} at REC1 dc terminals (see Fig. 1) can be computed with the same approach explained for u_{dcm1} provided that, in (1), the grid-side quantities (voltage V_g, pulsation ω_g, initial phase ϕ_{0g}), and firing angle of rectifiers switches α_g are considered instead of their motor-side counterparts V_m, ω_m, ϕ_{0m}, and α_m. Considering Fig. 10, $u_{\mathrm{dcg1}}(t)$ is determined as soon as voltages $v_{p1u1}^{0}\ (t)$ and $\Delta v_{p1u1}^{L}\ (t)$ are calculated according to their corresponding switching functions.

For LCI-drive systems featuring a dual three-phase arrangement [see Fig. 1(b) and (c)], the voltages at LCI2 and REC2 dc terminals need to be computed as well. For this purpose, the symmetrical operation of converters makes it possible to directly infer voltages u_{dcm2} and u_{dcg2} using the expressions found for u_{dcm1} and u_{dcg1} as follows:

$$u_{\mathrm{dcm2}}\left(t\right)=u_{\mathrm{dcm1}}\left(t+\frac{\pi}{6\omega_m}\right);\qquad u_{\mathrm{dcg2}}\left(t\right)=u_{\mathrm{dcg1}}\left(t+\frac{\pi}{6\omega_m}\right). \tag{27}$$

Also for the following, it is worth noting that the motor side parameters V_m, ω_m, ϕ_{0m}, and α_m and the grid-side parameters V_g, ω_g, ϕ_{0g}, and α_g are not totally decoupled and some constraints must be imposed to reflect a feasible drive operation.

In the real drive systems [see Fig. 2(a)], the grid-side firing angle α_g is dynamically changed by the control system to ensure that the dc-link current average value follows the reference one. Due to the negligible dc-link resistance, the average values of the dc-link voltages on the rectifier and inverter sides, must be necessarily equal. This leads to a constrained choice of α_g according to the following relationship:

$$\alpha_g = \operatorname{acos}\left\{\frac{V_m}{V_g}\cos\alpha_m\left[1+\frac{1}{2}\left(1+\frac{\omega_g L_{Cg}}{\omega_m L_{Cm}}\right)\right.\right.$$
$$\left.\left.\times\left(\sqrt{1+\frac{4\pi\omega_m L_{Cm} P_m}{9N\eta V_m^2\cos^2\alpha_m}}-1\right)\right]\right. \tag{28}$$

where P_m is the motor output (mechanical) power, N is the number of three-phase sets of the WFSM (N can be either 1 or 2 as explained in Section II-A) and η is the efficiency of the overall drive system (assumed equal to 97%), including both the WFSM and the LCI(s). The derivation of (28) is justified in Appendix C.

D. Experimental Validation

For assessment purposes, the analytical results for u_{dcm1} extracted with the proposed algebraic equations are next compared to the measurements carried out on the three different topologies shown in Fig. 1. Table IV shows the working points at which the measurements are recorded for the three configurations.

In Fig. 11, u_{dcm1} waveforms are shown for the operating points given in Table IV. According to this figure, there is an acceptable matching between predicted waveforms and measurements for the different operating points. However, some discrepancies arise due to different factors.

In order to explain the reason for the discrepancies, the harmonic spectra of the experimental dc-link voltage u_{dcm1} are compared to that of the analytical waveform. It is worth specifying that the spectral analysis is approximated owing to the necessarily limited time window (1 s) of the sample records, which causes all the noninteger harmonic frequencies to be affected by spectral leakage.

For the sake of brevity, the spectral analysis is presented only for the second [see Fig. 1(b)] and third [see Fig. 1(c)] LCI-fed drive system arrangements (in which the most significant discrepancies occur between analytical results and measurements). As expected, thanks to the assumption of smooth dc-link current, only the components of frequency $6\,k f_m$ ($k = 1, 2, 1/4$), with $f_m = 49.67$ Hz and $f_m = 40.8$ Hz for the second and third system arrangement respectively, are present in the spectra of the analytical dc-link voltage, shown in Figs. 12(a) and 13(a). On the other side, the experimental dc-link voltage, in addition to the harmonic components of frequency $6\,k f_m$, contains harmonic components of frequency $6\,k f_g$, as shown by the spectra in Figs. 12(b) and 13(b). This is due to the fact that the dc-link current is affected by a noticeable ripple, in which also harmonic components of frequency $6\,k f_g$ are included (see Section IV). These current harmonics produce voltage drops across the resistances and leakage inductances of the machine and of the connections between the machine and the measuring

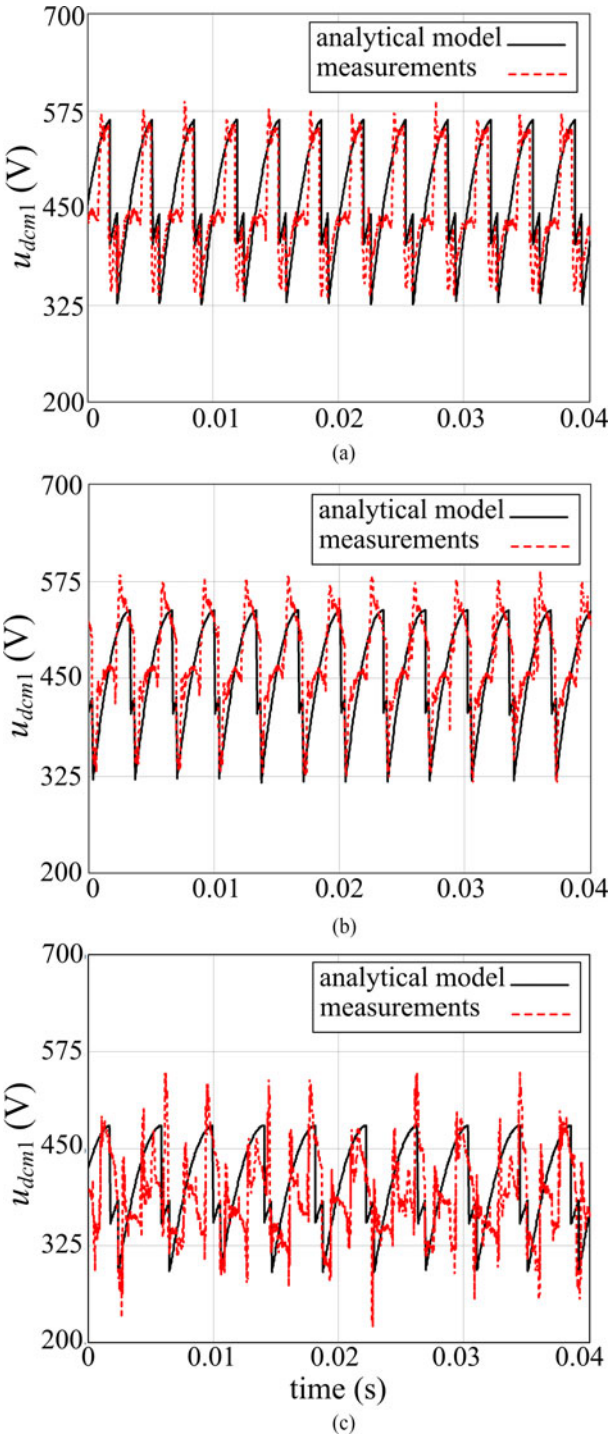

Fig. 11. u_{dcm1} waveforms for the three LCI-based drive topologies shown in Fig. 1: (a) single three-phase; (b) dual three-phase with separate dc links; (c) dual three-phase with interconnected dc links, with the operating points shown in Table IV.

cubicle (these connections are about 70 m long), which reflects in harmonics of frequency $6\,k f_g$ in the dc-link voltage.

The differences in the amplitudes of the dc-link voltage harmonic components of frequency $6\,k f_m$ in analytical waveforms and measurements are both due to the aforementioned voltage drops (neglected in the analytical model) and to the

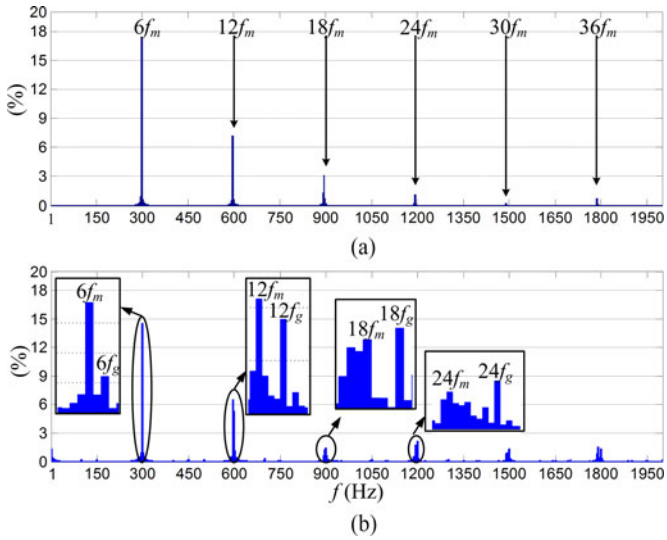

Fig. 12. Harmonic spectrum of the dc-link voltage, u_{dcm1}, shown in Fig. 11(b). The amplitude is expressed as a percentage of its dc value for (a) analytical approach ($U_{\mathrm{dc}} = 472$ V) and (b) experiments ($U_{\mathrm{dc}} = 480$ V).

uncertainties in the firing angle of the LCIs. In fact, in the LCI drive used for testing, the firing pulse timing is based on the voltage zero-crossing detection which, due to the highly distorted motor terminal voltages, suffers from inaccuracy. In this way the firing angle, which is set off-line to a reference value by the operator, is determined with an error of approximately $\pm 5°$. For instance, considering the second operating point of Table IV, if the firing angle is changed from 150° to 155° in the analytical model, the amplitude of the $6f_m$ harmonic decreases from 17% to 15%, thus almost nullifying the difference with the corresponding harmonic in the experimental spectrum.

IV. DC-Link Current Prediction

In this section, the dc-link current waveform will be derived from the various dc-link voltages obtained in the previous section.

For the sake of generality, the case of dual three-phase drive arrangements [see Fig. 1(b) and (c)], having the two dc-link currents i_{dc1}(t) and $i_{\mathrm{dc2}}(t)$, will be addressed, since the single three-phase configuration can be covered by simply considering $i_{\mathrm{dc1}}(t)$ only.

The dc-link currents $i_{\mathrm{dc1}}(t)$, $i_{\mathrm{dc2}}(t)$ include a constant component I_{dc} to which current pulsations $i_{\mathrm{ac1}}(t)$ and $i_{\mathrm{ac2}}(t)$ are superimposed

$$i_{\mathrm{dc1}}(t) = I_{\mathrm{dc}} + i_{\mathrm{ac1}}(t); \qquad i_{\mathrm{dc2}}(t) = I_{\mathrm{dc}} + i_{\mathrm{ac2}}(t). \tag{29}$$

The constant component I_{dc} is relatively easy to determine based on the power balance considerations developed in Appendix C, where the following expression is derived:

$$I_{\mathrm{dc}} = \frac{-\sqrt{3}V_m \cos\alpha_m + \sqrt{3V_m^2 \cos^2\alpha_m + (4\pi/3)(P_m/N\eta)\omega_m L_{Cm}}}{2\omega_m L_{Cm}}. \tag{30}$$

Conversely, current pulsations $i_{\mathrm{ac1}}(t)$ and $i_{\mathrm{ac2}}(t)$ are more difficult to determine but need to be found as they are responsible for a portion of torque pulsations. They relate to the voltage across the dc-link inductors ($v_{ind1}(t)$ and $v_{ind2}(t)$ in Fig. 1) through the following differential equations:

$$v_{ind1}(t) = L_{\mathrm{dc}} \frac{di_{\mathrm{ac1}}(t)}{dt}, \qquad v_{ind2}(t) = L_{\mathrm{dc}} \frac{di_{\mathrm{ac2}}(t)}{dt} \tag{31}$$

where L_{dc} is the inductance of the dc-link inductors. Since the voltage across the dc-link inductors can be easily found as the difference between the dc-link voltages at LCI and rectifier terminals (computed in Section III), the current pulsations could be theoretically obtained from (31) as

$$\begin{aligned} i_{\mathrm{ac1}}(t) &= i_{\mathrm{ac1}}(t_0) + \frac{1}{L_{\mathrm{dc}}}\int_{t_0}^{t} v_{ind1}(\tau)d\tau \\ i_{\mathrm{ac2}}(t) &= i_{\mathrm{ac2}}(t_0) + \frac{1}{L_{\mathrm{dc}}}\int_{t_0}^{t} v_{ind2}(\tau)d\tau \end{aligned} \tag{32}$$

for a given instant of time t_0, as usually done in dynamic simulation programs. One practical problem with this approach would be that the initial values $i_{\mathrm{ac1}}(t_0), i_{\mathrm{ac2}}(t_0)$ are unknown; the other problem is that (32) requires a numerical integration (which is time consuming), while the aim of this paper is to find an analytical (algebraic) formulation for all the quantities of interest at steady state.

Therefore, the methodology herein proposed to analytically find the dc-link current pulsation waveform at steady-state is based on the use of complex Fourier series expansions. To understand the form of these Fourier expansions, one should consider that, if f_g is the operating frequency of the grid-side ac quantities and f_m that of the motor-side ac quantities, then the harmonic spectrum of the ideal dc-link voltages at the rectifiers' output, $u_{\mathrm{dcg1}}(t)$ or $u_{\mathrm{dcg2}}(t)$, contain the frequencies $6\,kf_{\mathrm{g}}$ ($k = 1, 2, ...$) and the spectrum of the ideal dc-link voltages at the LCIs' input, $u_{\mathrm{dcm1}}(t)$ or $u_{\mathrm{dcm2}}(t)$, has the frequencies $6\,kf_m$ (by ideal dc-link voltage we mean that the dc-link current is assumed to be smooth, which implies that the dc-link voltages at the rectifiers' output are not affected by motor ac-side harmonics and that the dc-link voltages at the LCIs' input are not affected by grid ac-side harmonics). As a consequence, the voltage across the dc-link inductors $v_{ind1}(t)$ and $v_{ind2}(t)$ will generally have the frequency components $6\,kf_g$ and $6\,kf_m$ according to the superposition law (in particular, in the case of interconnected dc links, the frequencies $6\,kf_g$ and $6\,kf_m$ are canceled out for odd values of k [12]).

Based on these considerations, the two voltages $v_{ind1}(t)$ and $v_{ind2}(t)$ across the dc-link inductors can be expressed as

$$\begin{aligned} v_{ind1}(t) &= \sum_{n=-\infty}^{\infty} \bar{V}_{1gn} e^{in(2\pi f_g)t} + \sum_{n=-\infty}^{\infty} \bar{V}_{1mn} e^{in(2\pi f_m)t} \\ v_{ind2}(t) &= \sum_{n=-\infty}^{\infty} \bar{V}_{2gn} e^{in(2\pi f_g)t} + \sum_{n=-\infty}^{\infty} \bar{V}_{2mn} e^{in(2\pi f_m)t} \end{aligned} \tag{33}$$

where $\left(\bar{V}_{1gn}, \bar{V}_{1mn}\right)$ and $\left(\bar{V}_{2gn}, \bar{V}_{2mn}\right)$ are the *n*th complex Fourier coefficients of $v_{ind1}(t)$ and $v_{ind2}(t)$, respectively. The subscript "*m*" is used to indicate the coefficients resulting from motor-side converter operation and subscript "*g*" is used for the coefficients resulting from grid-side converter operation.

Similarly, the dc-link current pulsations can be expanded as

$$\begin{aligned} i_{\mathrm{ac1}}(t) &= \sum_{n=-\infty}^{\infty} \bar{I}_{1gn} e^{in(2\pi f_g)t} + \sum_{n=-\infty}^{\infty} \bar{I}_{1mn} e^{in(2\pi f_m)t} \\ i_{\mathrm{ac2}}(t) &= \sum_{n=-\infty}^{\infty} \bar{I}_{2gn} e^{in(2\pi f_g)t} + \sum_{n=-\infty}^{\infty} \bar{I}_{2mn} e^{in(2\pi f_m)t} \end{aligned} \tag{34}$$

where $\left(\bar{I}_{1gn}, \bar{I}_{1mn}\right)$ and $\left(\bar{I}_{2gn}, \bar{I}_{2mn}\right)$ are the *n*th complex Fourier coefficients of $i_{\mathrm{ac1}}(t)$ and $i_{\mathrm{ac2}}(t)$, respectively.

By replacing (33) and (34) into (31), the following relationships between the complex Fourier coefficients of dc-link voltages and currents are obtained:

$$\begin{aligned} \sum_{n=-\infty}^{\infty} \bar{V}_{1gn} e^{in\omega_g t} &= in\omega_g L_{\mathrm{dc}} \sum_{n=-\infty}^{\infty} \bar{I}_{1gn} e^{in\omega_g t} \\ \sum_{n=-\infty}^{\infty} \bar{V}_{1mn} e^{in\omega_m t} &= in\omega_m L_{\mathrm{dc}} \sum_{n=-\infty}^{\infty} \bar{I}_{1mn} e^{in\omega_m t} \\ \sum_{n=-\infty}^{\infty} \bar{V}_{2gn} e^{in\omega_g t} &= in\omega_g L_{\mathrm{dc}} \sum_{n=-\infty}^{\infty} \bar{I}_{2gn} e^{in\omega_g t} \\ \sum_{n=-\infty}^{\infty} \bar{V}_{2mn} e^{in\omega_m t} &= in\omega_m L_{\mathrm{dc}} \sum_{n=-\infty}^{\infty} \bar{I}_{2mn} e^{in\omega_m t}. \end{aligned} \tag{35}$$

Equation (35) shows that for any *n* different from zero

$$\begin{aligned} \bar{I}_{1gn} &= \frac{\bar{V}_{1gn}}{in\omega_g L_{dc}}, \qquad \bar{I}_{1mn} = \frac{\bar{V}_{1mn}}{in\omega_m L_{\mathrm{dc}}} \\ \bar{I}_{2gn} &= \frac{\bar{V}_{2gn}}{in\omega_g L_{\mathrm{dc}}}, \qquad \bar{I}_{2mn} = \frac{\bar{V}_{2mn}}{in\omega_m L_{\mathrm{dc}}} \end{aligned} \tag{36}$$

which gives the complex Fourier coefficients of the dc-link current for any *n* different from zero.

The problem is therefore reduced to computing the complex Fourier coefficients of the voltage across the dc-link inductors $v_{ind1}(t)$ and $v_{ind2}(t)$. These actually depend on the connections between the rectifiers and inverters so, to derive their expression, it is necessary to distinguish among the various drive configurations shown in Fig. 1. For the two topologies shown in Fig. 1(a) and (b) (single three-phase and dual three-phase with independent dc links), we can write

$$\begin{aligned} v_{ind1}(t) &= \left[u_{\mathrm{dcm1}}(t) - u_{\mathrm{dcg1}}(t)\right] \\ v_{ind2}(t) &= \left[u_{\mathrm{dcm2}}(t) - u_{\mathrm{dcg2}}(t)\right] \end{aligned} \tag{37}$$

where the second of the two equations obviously holds for the topology shown in Fig. 1(b) only.

For the configuration with interconnected dc links [see Fig. 2(c)], the dc-link current is the same for both LCI1 and LCI2 since they are connected in series. Consequently, the voltages across both dc-link inductors, i.e., $v_{ind1}(t)$ and $v_{ind2}(t)$, will be the same and given by

$$\begin{aligned} v_{ind1}(t) = \; v_{ind2}(t) = \tfrac{1}{2} \big[& u_{\mathrm{dcm2}}(t) + u_{\mathrm{dcm1}}(t) \\ & - u_{\mathrm{dcg2}}(t) - u_{\mathrm{dcg1}}(t) \big]. \end{aligned} \tag{38}$$

A. Complex Fourier Coefficients $\bar{V}_{1mn}$,$\bar{V}_{1gn}$ for Single Three-Phase and Dual-Three-Phase Configurations with Independent DC Links

For the drive arrangements given in Fig. 1(a) and (b), (37) holds. By definition of complex Fourier series coefficients, using (37) and (7) and the considerations made in Section III-C3, we can write

$$\begin{aligned} \bar{V}_{1mn} &= \frac{1}{T_m} \int_{t_0}^{t_0+T_m} u_{\mathrm{dcm1}}(\tau) e^{-in\omega_m \tau} d\tau \\ &= \frac{1}{T_m} \Bigg[\int_{t_0}^{t_0+T_m} v^0_{x1a1}(\tau) e^{-in\omega_m \tau} d\tau \\ &\quad + \int_{t_0}^{t_0+T_m} v^0_{x1a1}(\tau + \pi/\omega_m) e^{-in\omega_m \tau} d\tau \\ &\quad + \int_{t_0}^{t_0+T_m} \Delta v^L_{x1a1}(\tau) e^{-in\omega_m \tau} d\tau \\ &\quad + \int_{t_0}^{t_0+T_m} \Delta v^L_{x1a1}(\tau + \pi/\omega_m) e^{-in\omega_m \tau} d\tau \Bigg] \\ \bar{V}_{1gn} &= \frac{1}{T_g} \int_{t_0}^{t_0+T_g} u_{\mathrm{dcg1}}(\tau) e^{-in\omega_g \tau} d\tau \\ &= \frac{1}{T_g} \Bigg[\int_{t_0}^{t_0+T_g} v^0_{p1u1}(\tau) e^{-in\omega_g \tau} d\tau \\ &\quad + \int_{t_0}^{t_0+T_g} v^0_{p1u1}(\tau + \pi/\omega_g) e^{-in\omega_g \tau} d\tau \\ &\quad + \int_{t_0}^{t_0+T_g} \Delta v^L_{p1u1}(\tau) e^{-in\omega_g \tau} d\tau \\ &\quad + \int_{t_0}^{t_0+T_g} \Delta v^L_{p1u1}(\tau + \pi/\omega_g) e^{-in\omega_g \tau} d\tau \Bigg] \end{aligned} \tag{39}$$

where $T_m = 1/f_m, T_g = 1/f_g$, and t_0 is a generic instant of time.

Here the procedure to compute integrals in (39), including $v^0_{x1a1}(\tau)$ and $\Delta v^L_{x1a1}(\tau)$, is explained in detail since the calculation of the integrals including $v^0_{p1u1}(\tau)$ and $\Delta v^L_{p1u1}(\tau)$ can be performed similarly by simply replacing the motor-side quantities with the grid-side ones. In other words, the complex quantities

$$\bar{C}^m_n = \frac{1}{T_m} \int_{t_0}^{t_0+T_m} v^0_{x1a1}(\tau)\, e^{-in\omega_m \tau} d\tau \tag{40}$$

$$\bar{D}^m_n = \frac{1}{T_m} \int_{t_0}^{t_0+T_m} \Delta v^L_{x1a1}(\tau) e^{-in\omega_m \tau} d\tau \tag{41}$$

have to be calculated.

For this purpose, explicit expressions for $v^0_{x1a1}(t)$ and $\Delta v^L_{x1a1}(t)$ have been derived in Section III as per (12) and (24) in terms of the switching matrices $\mathbf{S}_0$ and $\mathbf{S}_\mathrm{L}$, the functions $f(\theta)$ and $g(\theta)$ and the vector of motor-side voltages $\mathbf{v}_{\mathrm{m}1}(t)$. The latter, given by (9), can be expressed in complex form as follows:

$$\mathbf{v}_{m1}(t) = \mathbf{A}e^{i\omega_m t} - \mathbf{B}e^{-i\omega_m t} \tag{42}$$

where matrices $\mathbf{A}$ and $\mathbf{B}$ are given by

$$\mathbf{A} = \frac{V_m}{i2}\begin{pmatrix} e^{-i\phi_{0m}} - e^{-i\left(\frac{2\pi}{3}+\phi_{0m}\right)} \\ e^{-i\left(\frac{2\pi}{3}+\phi_{0m}\right)} - e^{-i\left(\frac{4\pi}{3}+\phi_{0m}\right)} \\ e^{-i\left(\frac{4\pi}{3}+\phi_{0m}\right)} - e^{-i\phi_{0m}} \end{pmatrix}$$

$$\mathbf{B} = \frac{V_m}{i2}\begin{pmatrix} e^{i\phi_{0m}} - e^{i\left(\frac{2\pi}{3}+\phi_{0m}\right)} \\ e^{i\left(\frac{2\pi}{3}+\phi_{0m}\right)} - e^{i\left(\frac{4\pi}{3}+\phi_{0m}\right)} \\ e^{i\left(\frac{4\pi}{3}+\phi_{0m}\right)} - e^{i\phi_{0m}} \end{pmatrix}. \tag{43}$$

Therefore, a primitive function (or indefinite integral) of $\mathbf{v}_{m1}(\tau)\, e^{-in\omega_m \tau}$ will be of the form

$$\Im_{m1}(\tau) = \int \mathbf{v}_{m1}(\tau)\, e^{-in\omega_m \tau} d\tau = \begin{cases} \mathbf{A}\tau - \dfrac{1}{-2i\omega_m}\mathbf{B}e^{-2i\omega_m \tau} & n = 1 \\ \dfrac{\mathbf{A}e^{i\omega_m(1-n)\tau}}{i\omega_m(1-n)} - \dfrac{\mathbf{B}e^{-i\omega_m(1+n)\tau}}{-i\omega_m(1+n)} & n \neq 1. \end{cases} \tag{44}$$

At this point, the integration interval, ranging from t_0 to $t_0 + T_m$, can be subdivided into the four subintervals marked with letters *A*, *B*, *C*, *D* in Fig. 14 so that (40) can be written as

$$\begin{aligned} \bar{C}^m_n &= \frac{1}{T_m}\int_{t_0}^{t_0+T_m} v^0_{x1a1}(\tau)\, e^{-in\omega_m \tau} d\tau \\ &= \frac{1}{T_m}\left(I^0_A + I^0_B + I^0_C + I^0_D\right) \end{aligned} \tag{45}$$

where $I^0_A, I^0_B, I^0_C, I^0_D$ denote the integrals extended over the intervals *A*, *B*, *C*, *D* in Fig. 14.

In Fig. 14, $j_{m,p}$ indicates the conduction interval $Sj_{m,p}$ where t_0 is placed. Determination of $j_{m,p}$ is explained in Appendix D.

Based on these definitions and using (12) and (44), the terms $I^0_A, I^0_B, I^0_C, I^0_D$ in (45) take the form

$$\begin{aligned} I^0_A &= \int_{t_0}^{t_1} v^0_{x1a1}(\tau)\, e^{-in\omega_m \tau} d\tau \\ &= \left\{\mathbf{S}_0\left[\Im_{m1}\left(\frac{\theta_{0m} + j_{m,p}\pi/3}{\omega_m}\right) - \Im_{m1}(t_0)\right]\right\}_{j_{m,p}} \end{aligned} \tag{46}$$

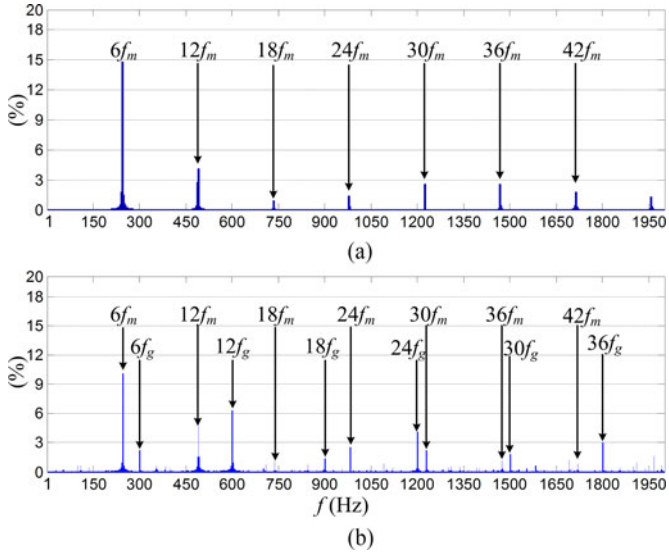

Fig. 13. Harmonic spectrum of the dc-link voltage, $u_{\mathrm{dcm}1}$, shown in Fig. 12(c) (the amplitude is expressed as a percentage of the dc value) for (a) analytical approach ($U_{\mathrm{dc}} = 396$ V) and (b) experiments ($U_{\mathrm{dc}} = 388$ V).

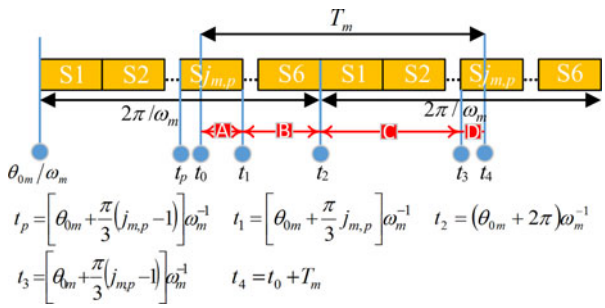

Fig. 14. Example of conduction intervals, which could be placed within a generic time interval $(t_0\, t_0 + T_m)$.

$$\begin{aligned} I^0_B &= \int_{t_1}^{t_2} v^0_{x1a1}(\tau)\, e^{-in\omega_m \tau} d\tau \\ &= \sum_{j_{m,p} < j_m \le 6}\left\{\mathbf{S}_0\left[\Im_{m1}\left(\frac{\theta_{0m} + j_m \pi/3}{\omega_m}\right)\right.\right. \\ &\quad \left.\left. - \Im_{m1}\left(\frac{\theta_{m0} + (j_m - 1)\pi/3}{\omega_m}\right)\right]\right\}_{j_m} \end{aligned} \tag{47}$$

$$\begin{aligned} I^0_C &= \int_{t_2}^{t_3} v^0_{x1a1}(\tau)\, e^{-in\omega_m \tau} d\tau \\ &= \sum_{1 \le j_m < j_{m,p}}\left\{\mathbf{S}_0\left[\Im_{m1}\left(\frac{\theta_{0m} + j_m \pi/3 + 2\pi}{\omega_m}\right)\right.\right. \\ &\quad \left.\left. - \Im_{m1}\left(\frac{\theta_{0m} + (j_m - 1)\pi/3 + 2\pi}{\omega_m}\right)\right]\right\}_{j_m} \end{aligned} \tag{48}$$

$$\begin{aligned} I^0_D &= \int_{t_3}^{t_4} v^0_{x1a1}(\tau)\, e^{-in\omega_m \tau} d\tau = \left\{\mathbf{S}_0\left[\Im_{m1}(t_0 + T_m)\right.\right. \\ &\quad \left.\left. - \Im_{m1}\left(\frac{\theta_{0m} + (j_{m,p} - 1)\pi/3 + 2\pi}{\omega_m}\right)\right]\right\}_{j_{m,p}}. \end{aligned} \tag{49}$$

Similarly, (41) canbe written as the sum of four terms as

$$\begin{aligned}\bar{D}_n^m &= \frac{1}{T_m}\int_{t_0}^{t_0+T_m}\Delta v_{x1a1}^L(\tau)e^{-in\omega_m\tau}d\tau \\ &= \frac{1}{T_m}\left(I_A^L+I_B^L+I_C^L+I_D^L\right)\end{aligned} \tag{50}$$

where $I_A^L, I_B^L, I_C^L, I_D^L$ denote the integrals extended over the ranges *A, B, C, D* shown in Fig. 14, where the conduction intervals S1 . . . S6 are replaced by the commutation intervals C1 . . . C6 (see Fig. 4). Keeping in mind (24) and (44) and knowing that the generic commutation interval C$j_{\rm m}$ has the same starting point of the conduction interval Sj_m but its duration is μ_m/ω_m instead of $\pi/3\omega_m$ (see Fig. 4), one can easily find the expression for the terms I_A^L (bottom of the page), I_B^L, I_C^L, and I_D^L (bottom of the page) in (equations (51)–(53) shown at the bottom of the page.

At this point, the overall integral (39) can be evaluated analytically as equation (54)–(55) shown at the bottom of the page where the terms

$$\begin{aligned}\bar{C}_n^g &= \frac{1}{T_g}\int_{t_0}^{t_0+T_g} v_{p1u1}^0(\tau)e^{-in\omega_g\tau}d\tau \\ \bar{D}_n^g &= \frac{1}{T_g}\int_{t_0}^{t_0+T_g}\Delta v_{p1u1}^L(\tau)e^{-in\omega_g\tau}d\tau\end{aligned} \tag{56}$$

can be computed with the same procedure described for $\bar{C}_n^m$, $\bar{D}_n^m$, applied to grid-side quantities, and where the following relationships are used:

$$\begin{aligned}\bar{C}_n^m e^{in\pi} &= \frac{1}{T_m}\int_{t_0}^{t_0+T_m} v_{x1a1}^0(\tau+\pi/\omega_m)e^{-in\omega_m\tau}d\tau \\ \bar{D}_n^m e^{in\pi} &= \frac{1}{T_m}\int_{t_0}^{t_0+T_m}\Delta v_{x1a1}^L(\tau+\pi/\omega_m)e^{-in\omega_m\tau}d\tau\end{aligned} \tag{57}$$

$$\begin{aligned}\bar{C}_n^g e^{in\pi} &= \frac{1}{T_g}\int_{t_0}^{t_0+T_g} v_{p1u1}^0(\tau+\pi/\omega_g)e^{-in\omega_g\tau}d\tau \\ \bar{D}_n^g e^{in\pi} &= \frac{1}{T_g}\int_{t_0}^{t_0+T_g}\Delta v_{p1u1}^L(\tau+\pi/\omega_g)e^{-in\omega_g\tau}d\tau.\end{aligned} \tag{58}$$

B. Complex Fourier Coefficients $\bar{V}_{2gn}$, $\bar{V}_{2mn}$ for Dual-Three Phase Configurations with Independent DC Links

The complex Fourier coefficients $\bar{V}_{2gn}, \bar{V}_{2mn}$ for the voltage $v_{ind2}(t)$ given by (37) are obtained exactly as the coefficients $\bar{V}_{1mn}, \bar{V}_{1gn}$ except that LCI2 and REC2 are considered instead of LCI1 and REC1.

C. Complex Fourier Coefficients $\bar{V}_{gn}$,$\bar{V}_{mn}$ for the Dual Three-Phase Configurations with Interconnected DC Links

Since the dc links are connected in the interconnected configuration, one set of Fourier coefficients are considered for the

$$I_A^L = \begin{cases}\int_{t_0}^{t_1}\Delta v_{x1a1}^L(\tau)\,e^{-in\omega_m\tau}d\tau = \left\{\mathbf{S}_L\left[\Im_{m1}\left(\dfrac{\theta_{0m}+(j_{m,p}-1)\,\pi/3+\mu_m}{\omega_m}\right)-\Im_{m1}(t_0)\right]\right\}_{j_{m,p}} & \text{if} \quad t_0 < t_p+\frac{\mu_m}{\omega_m} \\ 0, & \text{otherwise}\end{cases} \tag{51}$$

$$I_B^L = \int_{t_1}^{t_2}\Delta v_{x1a1}^L(\tau)\,e^{-in\omega_m\tau}d\tau = \sum_{j_{m,p}<j_m\le 6}\left\{\mathbf{S}_L\left[\Im_{m1}\left(\frac{\theta_{m0}+(j_m-1)\,\pi/3+\mu_m}{\omega_m}\right)-\Im_{m1}\left(\frac{\theta_{m0}+(j_m-1)\,\pi/3}{\omega_m}\right)\right]\right\}_{j_m} \tag{52}$$

$$\begin{aligned}I_C^L = \int_{t_2}^{t_3}\Delta v_{x1a1}^L(\tau)\,e^{-in\omega_m\tau}d\tau = \sum_{1\le j_m<j_{m,p}}\Bigg\{\mathbf{S}_L\Bigg[&\Im_{m1}\left(\frac{\theta_{0m}+(j_m-1)\,\pi/3+\mu_m+2\pi}{\omega_m}\right) \\ &-\Im_{m1}\left(\frac{\theta_{0m}+(j_m-1)\,\pi/3+2\pi}{\omega_m}\right)\Bigg]\Bigg\}_{j_m}\end{aligned} \tag{53}$$

$$I_D^L = \begin{cases}\int_{t_3}^{t_4}\Delta v_{x1a1}^L(\tau)\,e^{-in\omega_m\tau}d\tau = \left\{\mathbf{S}_L\left[\Im_{m1}(t_0+T_m)-\Im_{m1}\left(\frac{\theta_{0m}+(j_{m,p}-1)\pi/3+2\pi}{\omega_m}\right)\right]\right\}_{j_{m,p}} & \text{if } t_4 < t_3+\frac{\mu_m}{\omega_m} \\ \int_{t_3}^{t_3+\frac{\mu_m}{\omega_m}}\Delta v_{x1a1}^L(\tau)\,e^{-in\omega_m\tau}d\tau = \left\{\mathbf{S}_L\left[\Im_{m1}\left(\frac{\theta_{0m}+(j_{m,p}-1)\pi/3+\mu_m+2\pi}{\omega_m}\right)-\Im_{m1}\left(\frac{\theta_{0m}+(j_{m,p}-1)\pi/3+2\pi}{\omega_m}\right)\right]\right\}_{j_{m,p}} & \text{if } t_4 \ge t_3+\frac{\mu_m}{\omega_m}\end{cases} \tag{54}$$

$$\begin{aligned}\bar{V}_{1gn} &= \bar{C}_n^g+\bar{D}_n^g+\bar{C}_n^g e^{in\pi}+\bar{D}_n^g e^{in\pi} \\ \bar{V}_{1mn} &= \bar{C}_n^m+\bar{D}_n^m+\bar{C}_n^m e^{in\pi}+\bar{D}_n^m e^{in\pi}\end{aligned} \tag{55}$$

LCIs input voltages as $\bar{V}_{mn}$ and another for the rectifiers output voltages as $\bar{V}_{gn}$. Hence, according to (38), we have

$$\bar{V}_{mn} = \frac{1}{T_m}\int_{t_0}^{t_0+T_m} \tfrac{1}{2}\left[u_{\mathrm{dcm2}}(\tau)+u_{\mathrm{dcm1}}(\tau)\right] e^{-in\omega_m\tau}\,d\tau$$
$$\bar{V}_{gn} = \frac{1}{T_g}\int_{t_0}^{t_0+T_g} \tfrac{1}{2}\left[u_{\mathrm{dcg2}}(\tau)+u_{\mathrm{dcg1}}(\tau)\right] e^{-in\omega_g\tau}\,d\tau. \tag{59}$$

Similar to the procedure described in Section IV-A, the final equations for $\bar{V}_{mn}$ and $\bar{V}_{gn}$ are

$$\bar{V}_{mn} = \frac{\bar{C}_n^m + \bar{D}_n^m + \bar{C}_n^m e^{in\pi} + \bar{D}_n^m e^{in\pi}}{2} + \frac{e^{in\frac{\pi}{6}}\left(\bar{C}_n^m + \bar{D}_n^m + \bar{C}_n^m e^{in\pi} + \bar{D}_n^m e^{in\pi}\right)}{2}$$
$$\bar{V}_{gn} = \frac{\left(\bar{C}_n^g + \bar{D}_n^g + \bar{C}_n^g e^{in\pi} + \bar{D}_n^g e^{in\pi}\right)}{2} + \frac{e^{in\frac{\pi}{6}}\left(\bar{C}_n^g + \bar{D}_n^g + \bar{C}_n^g e^{in\pi} + \bar{D}_n^g e^{in\pi}\right)}{2} \tag{60}$$

D. DC-Link Current Computation

Once the coefficients $\left(\bar{V}_{1mn}, \bar{V}_{1gn}\right)$, $\left(\bar{V}_{2mn}, \bar{V}_{2gn}\right)$, or $\left(\bar{V}_{mn}, \bar{V}_{gn}\right)$ are computed as described in Sections IV-A, IV-B, and IV-C, the complex Fourier coefficients of the dc-link current are also known from (36) and the current pulsations from (34). The overall dc-link current then results from summing the current pulsation to the constant component (30) as per (29).

E. Experimental Validation

Fig. 15 shows the comparison between the dc-link current waveforms obtained with the analytical approach described above and the measurements. The waveforms are extracted under the operating conditions stated in Table IV for the three different configurations. It can be seen that a satisfactory matching is achieved between analytical prediction and current recordings.

The harmonic spectra of the experimental and analytical dc-link current are shown in Figs. 16 and 17 for the separate and interconnected dc-link configuration, respectively. As expected, observing the dc-link current waveforms [see Fig. 15(b) and (c)], a good accordance is observable between the experimental and analytical spectra. Harmonic components in the analytical dc-link current result from the application of the superposition law. Therefore, it can be deduced that the presence of $6\,kf_m$ and $6\,kf_g$ harmonic frequencies in Fig. 16(a) and $12\,kf_m$ and $12\,kf_g$ in Fig. 17(a) is due to the independent operation of LCIs and rectifiers, respectively. This is not true for the experimental dc-link current. However, the limited discrepancies between the amplitude of the harmonic components in the analytical and experimental spectra testify that the $6\,kf_m$ and $12\,kf_m$ harmonic frequencies are mainly due to the LCIs operation, while the $6\,kf_g$ and $12\,kf_g$ harmonic frequencies are mainly due to the rectifiers operation.

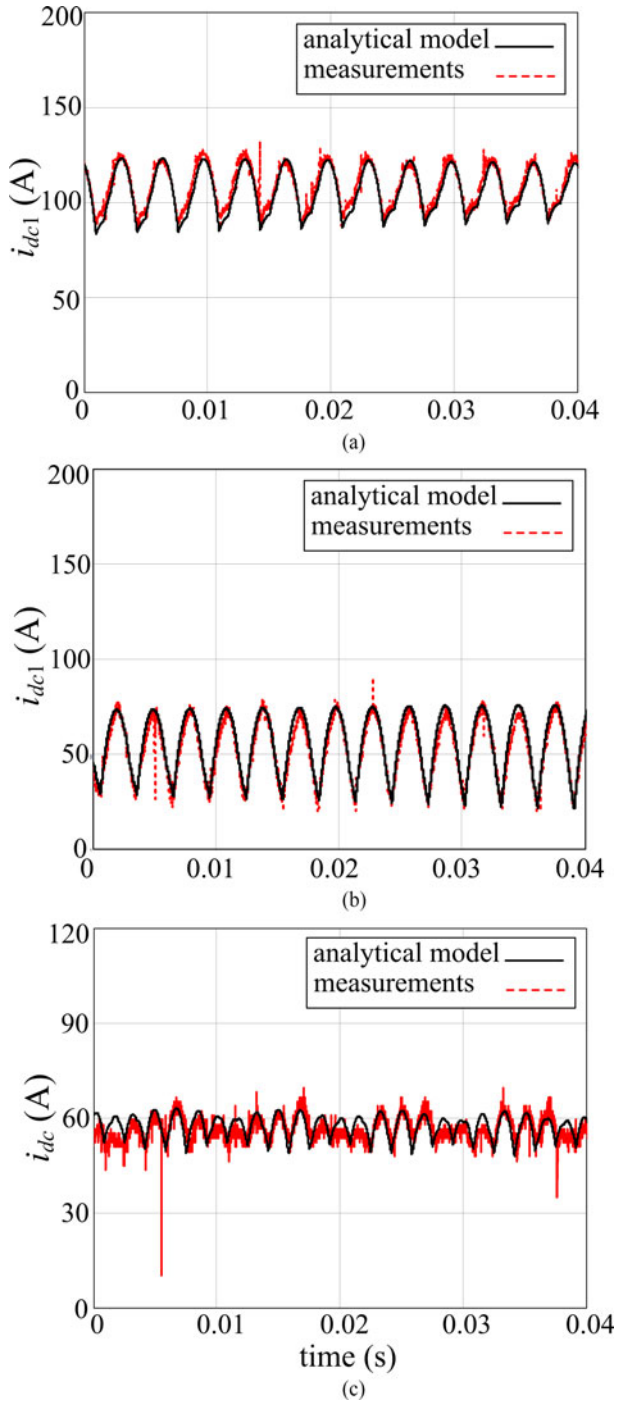

Fig. 15. DC-link current i_{dc1} for the three LCI-fed drive topologies shown in Fig. 1 with the operating points shown in Table IV: (a) single three-phase; (b) dual three-phase with separate dc links; and (c) dual three-phase with interconnected dc links.

Thanks to the interconnected dc-link arrangement only harmonic components of frequency $12\,kf_m$ and $12\,kf_g$ can be found in the spectrum of Fig. 17(a). However, in the spectrum of the experimental waveform, shown in Fig. 17(b), also components of frequency $6\,kf_g$ (in particular $6f_g$ and $18f_g$) have amplitudes different from zero. This results from the independent control of the two rectifiers [see Fig. 2(a)], which introduces slight

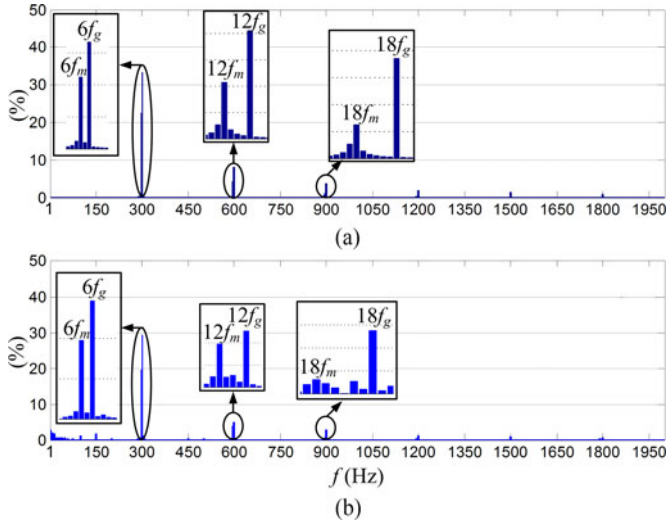

Fig. 16. Harmonic spectrum of the dc-link current, i_{dc1}, shown in Fig. 15(b) relative to its dc value for (a) analytical approach ($I_{\mathrm{dc}} = 52\,\mathrm{A}$) and (b) experiments ($I_{\mathrm{dc}} = 52\,\mathrm{A}$).

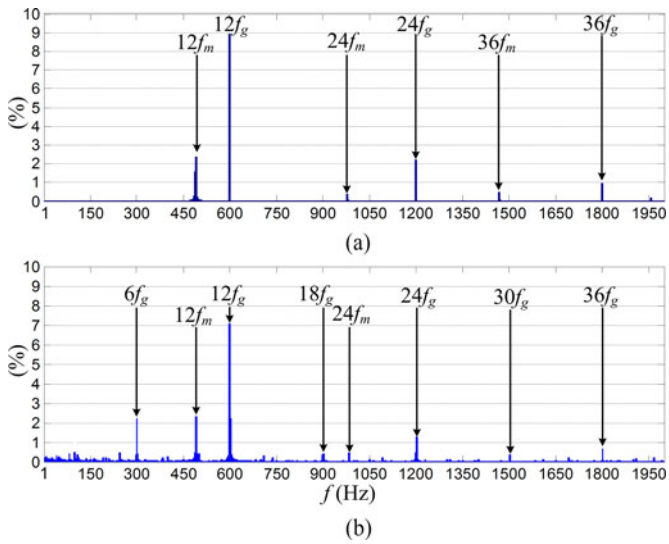

Fig 17. Harmonic spectrum of the dc-link current, i_{dc1}, shown in Fig. 15(c) relative to its dc value for (a) analytical approach ($I_{\mathrm{dc}} = 57\,\mathrm{A}$) and (b) experiments ($I_{\mathrm{dc}} = 57\,\mathrm{A}$).

differences in the firing angles, thus causing the not complete cancellation of the harmonic components of frequency $6\,k f_g$ (with k being an odd integer). This phenomenon is better discussed in the next subsection dealing with the torque, where simulation results are provided to support the thesis that a difference in the firing angles leads to the appearance of frequency components that should be theoretically null in case of ideal operation.

V. Torque Prediction

The torque of the machine is defined as the mechanical power transferred to the shaft divided by the speed [16]. Disregarding the conduction drops of the switches, the power delivered to the shaft is equal to the electrical power entering the LCI(s) feeding

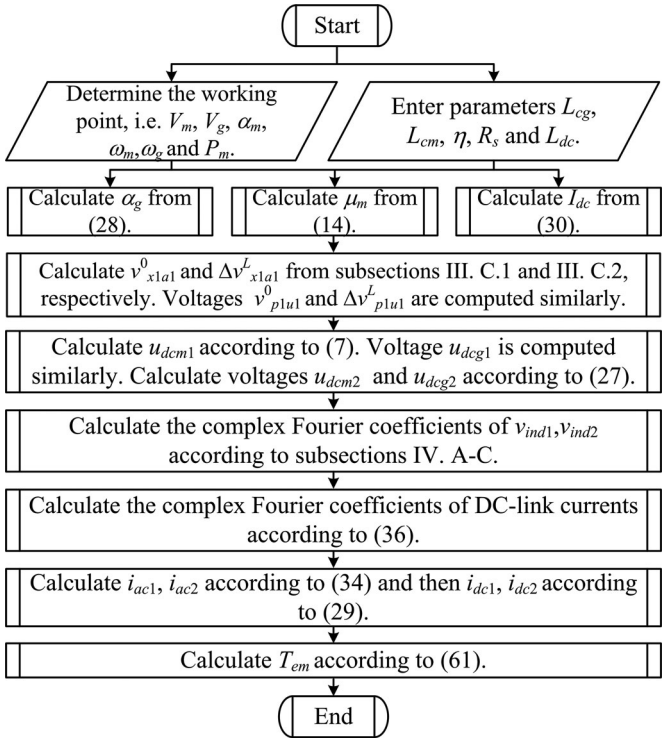

Fig. 18. Flowchart of the proposed algebraic method.

the WFSM after subtracting the stator joule losses. This leads to the following torque expression:

$$T_{em}(t) = \frac{p\left[i_{\mathrm{dc1}}(t)u_{\mathrm{dcm1}}(t) + i_{\mathrm{dc2}}(t)u_{\mathrm{dcm2}}(t)\right]}{\omega_m} - \frac{pP_{\mathrm{loss}}}{\omega_m} \tag{61}$$

where p is the number of machine pole pairs and P_{loss} represents the stator joule losses. Also, $i_{\mathrm{dc1}}(t)$ and $i_{\mathrm{dc2}}(t)$ are the dc-link currents (see Fig. 1) computed as per Section IV and $u_{\mathrm{dcm1}}(t)$ and $u_{\mathrm{dcm2}}(t)$ are the LCI input dc voltages computed as discussed in Section III. As regards the losses in the stator winding, we can write

$$P_{\mathrm{loss}} = 3NR_s\left(\kappa I_{\mathrm{dc}}\right)^2 \tag{62}$$

where the term κI_{dc} is the rms value of the fundamental component of stator phase current and $N = 2$ is the number of stator three-phase sets. Assuming an ideal rectangular waveform for the phase current (i_{a1} in Fig. 5), we have $\kappa = \sqrt{6/\pi}$ [20].

To sum up, the proposed algebraic modeling approach to compute the machine electromagnetic torque is illustrated step by step in the flowchart shown in Fig. 18.

In Fig. 19, $T_{em}(t)$ calculated by (61) is compared with the results acquired from a torque meter mounted on the machine shaft, showing an overall satisfactory matching.

The harmonic spectra of the analytical and experimental torque waveforms shown in Fig. 19(b) and (c) are plotted in Figs. 20 and 21, respectively. Comparison of the analytical spectra with the experimental ones shows that the main harmonics are the same and their amplitudes are satisfactorily matching. The main harmonics of both the interconnected dc-link and

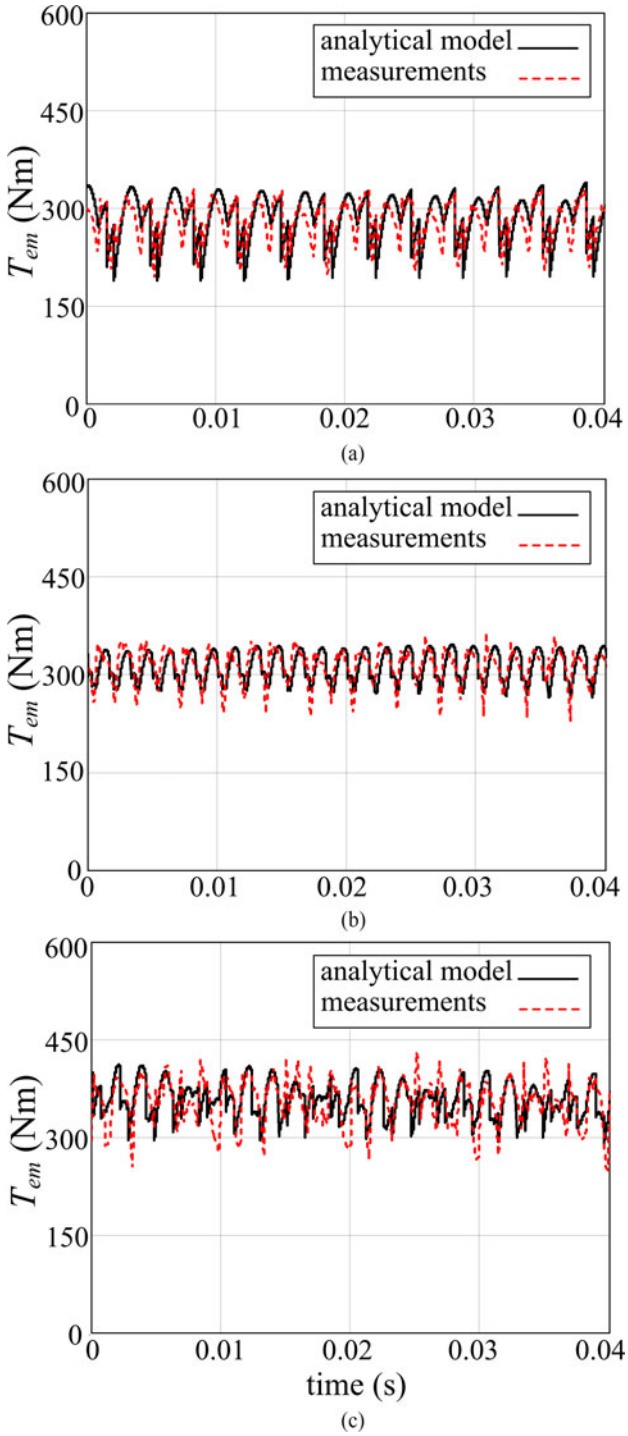

Fig. 19. Electromagnetic torque T_{em} for the three LCI-fed drive topologies shown in Fig. 1 with the operating points shown in Table IV: (a) single three-phase; (b) dual three-phase with separate dc links; and (c) dual three-phase with interconnected dc links.

the separate dc-link arrangements have frequencies $12\,kf_m$ and $12\,kf_g$. Harmonic frequencies $6\,kf_m$ and $6\,kf_g$ (with k being an odd integer) should not be found also in torque spectrum of the separate dc-link configuration, thanks, respectively, to the 30° displacement of the two-motor three-phase winding sets and the 30 electrical degrees displacements of the three-phase voltages supplying the two rectifiers.

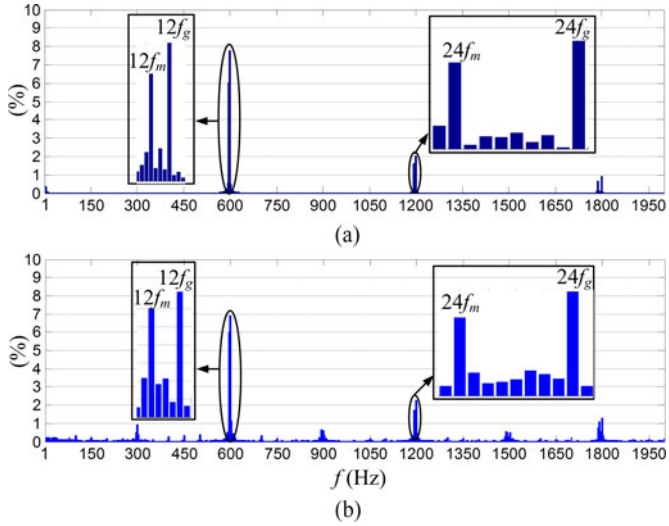

Fig. 20. Harmonic spectrum of the torque, T_{em}, shown in Fig. 19(b) relative to its average value for (a) analytical approach ($T_{\rm ave} = 321\,{\rm N\cdot m}$) and (b) experiments ($T_{\rm ave} = 324\,{\rm N\cdot m}$).

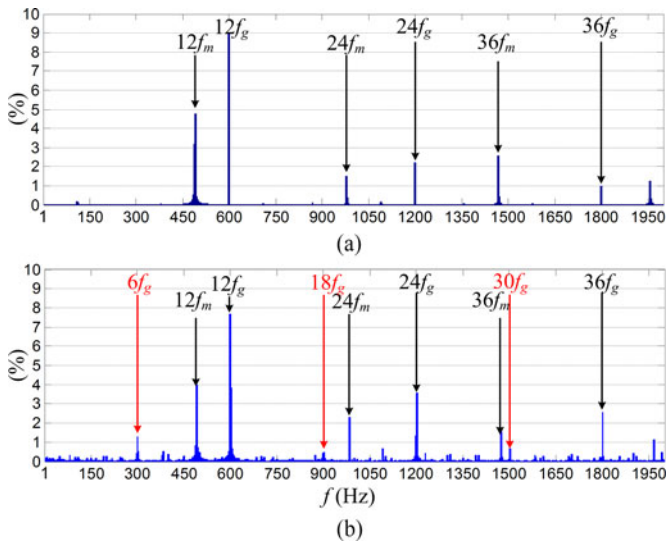

Fig. 21. Harmonic spectrum of the torque, T_{em}, shown in Fig. 19(c) relative to its average value for (a) analytical approach ($T_{\rm ave} = 361\,{\rm N\cdot m}$) and (b) experiments ($T_{\rm ave} = 356\,{\rm N\cdot m}$).

Actually, in the spectra of the experimental waveforms, shown in Figs. 20(b) and 21(b), also components of frequency $6\,kf_g$ have amplitude different from zero, even if their amplitudes are very small with respect to the main harmonics. This is due to the presence of $6\,kf_g$ (with k odd integer) frequency components in the spectrum of the dc-link current, owing to the aforementioned slight differences in the independently controlled firing angles of the two rectifiers.

The effect of differences in the firing angles of the two rectifiers can be analyzed by the analytical model, setting the firing angle α_{g2} different from α_{g1}. Fig. 22 shows how even a small difference between α_{g2} and α_{g1} causes the harmonics of frequency $6\,kf_g$ (with k odd integer) to appear in the spectrum

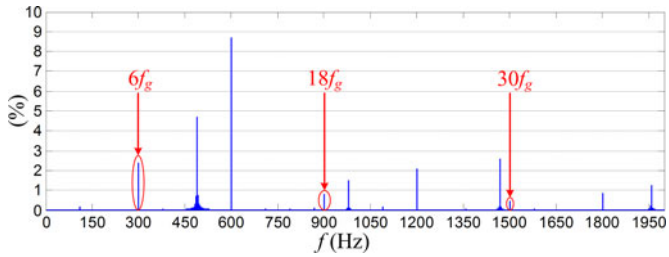

Fig. 22. Harmonic spectrum of the analytical torque relative to the dc component when the firing angles of the two rectifiers are different, i.e., $\alpha_{g2} = \alpha_{g1} + 2$, in the third operating point of Table IV.

TABLE V
RATINGS OF THE MACHINE USED IN DYNAMIC SIMULATIONS

Apparent Power	1 MVA	Stator Phase Current	1034 A
Line-to-Line Voltage	570 V	Speed	300 r/min

TABLE VI
MACHINE PARAMETERS USED FOR DYNAMIC MODELING

Stator resistance r_s	1.8 mΩ	d-Axis leakage inductance L_{lkd} [a]	0.015
Excitation resistance r_f [a]	0.6 mΩ	q-Axis leakage inductance L_{lkq} [a]	0.024
d-Axis resistance r_{kd} [a]	5.1 mΩ	d-Axis magnetizing inductance L_{md}	0.63
q-Axis resistance r_{kq} [a]	8.6 mΩ	q-Axis magnetizing inductance L_{mq}	0.54
Stator leakage inductance L_{ls}	0.07 mH	Number of pole pairs p	2
Excitation leakage inductance L_{lf} [a]	0.05 mH	Moment of inertia J	100 kg·m^2

Load characteristics: Frictional, with torque given by $T_l = K_l \omega_m$, $K_l = 10.2$ N·m·s/rad (ω_m being the mechanical speed).
[a]Rotor parameters are referred to the stator.

TABLE VII
PI REGULATOR COEFFICIENTS IN THE SIMULATIONS

Regulator	Proportional Gain	Integral Gain
Speed controller	60	8955
DC-link current controller	0.005	0.746
Excitation current controller	0.19	2.26

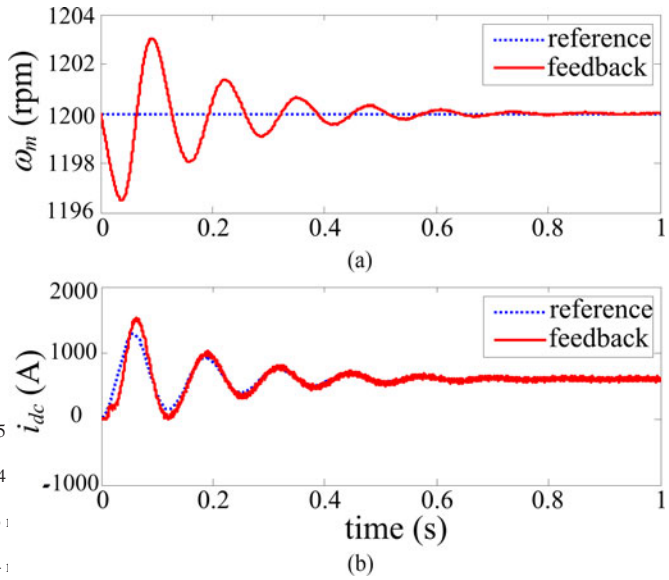

Fig. 23. Simulation results for reference and real values of (a) rotor mechanical speed and (b) dc-link current.

of the analytical torque. In the example of Fig. 22, where $\alpha_{g2} = \alpha_{g1} + 2$, the amplitude of the harmonics of frequency $6\,f_g$ and $18 f_g$ is even higher than the corresponding harmonics in the spectrum of the experimental torque [see Fig. 21(b)].

VI. EVALUATION OF THE PROPOSED METHOD EFFECTIVENESS COMPARED TO THE DYNAMIC SIMULATIONS

In order to better highlight the computational effort of dynamic numerical simulations compared to the proposed analytical approach, a complete high-power three-phase LCI-fed WFSM drive system is implemented in MATLAB/Simulink environment. Ratings of the machine are mentioned in Table V. Also, a complete list of parameters which are essential to construct the dynamic model is given in Table VI. It can be seen that, contrary to the proposed analytical model, dynamic simulation requires the knowledge of a large amount of parameters. A set of seven differential equations including those for the three stator $dq0$ circuits, three rotor circuits (excitation, d-axis and q-axis dampers), and the equation of rotor motion are to be implemented to model the behavior of the machine [16]. As regards the control section, three PI regulators (see Table VII) are needed to control speed, dc-link and field currents (a three-phase thyristor bridge rectifier is used to feed the field current) [20]. The adjustment of the proportional and integral coefficients for the three regulators to achieve a good dynamic response may also be troublesome [22], [23].

As mentioned previously, it may take a relatively long time for the dynamic simulation to reach steady-state conditions. For instance, the reference values of the machine speed and dc-link current (which is the output of the speed PI regulator) are compared to their actual values in Fig. 23. In the simulations, the speed reference is set to 0.4 pu. Also the speed initial condition is set to 0.4 p.u. in the motion equation to minimize the settling time and inhibit possible system instability. Fig. 23 shows that the required time for the actual speed to reach the steady-state value is around 1 s. The measured real time to finish 1 s of simulation is around 90 s while the analytical model takes less than 1 s to give the desired steady-state results on the same computer.

In Fig. 24, the simulation results for the steady-state waveforms of $i_{\mathrm{dc}}(t), u_{\mathrm{dcm}}(t)$, and $T(t)$ are compared to the analytical model outputs. The steady-state quantities are $\omega_m = 1200\,\mathrm{r/min}$ (mechanical), $\alpha_m = 145, \alpha_g = 68, \mu_m = 7.2, I_{\mathrm{dc}} = 600\,\mathrm{A}, V_m = 202\,\mathrm{V}$, and $V_g = 473\,\mathrm{V}$.

It can be seen that analytical predictions are in better accordance with simulation results than with measurements. This is due to several reasons. For example, in the simulations the machine stator fluxes extracted from the machine model are utilized

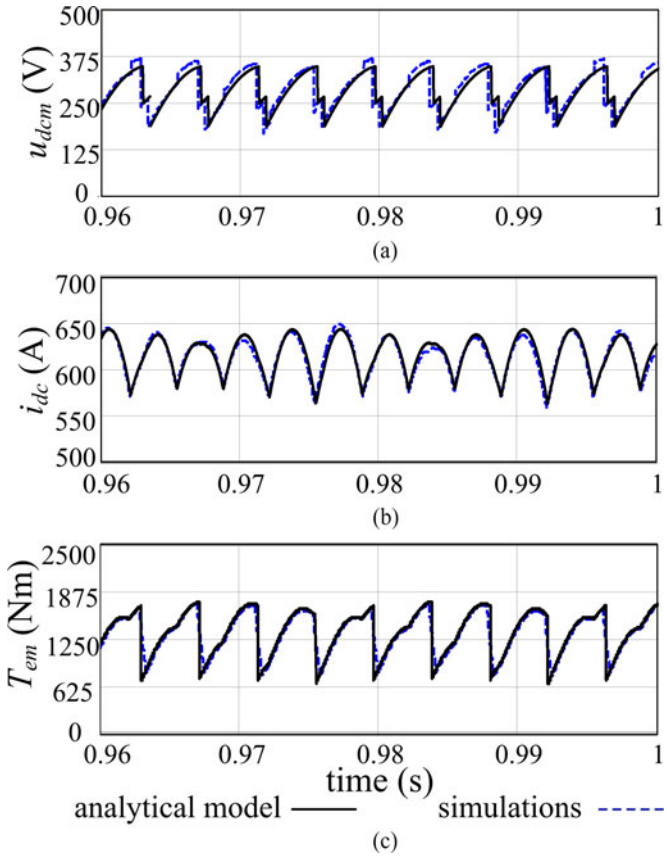

Fig. 24. Comparison between simulation and analytical results for a three-phase LCI drive steady-state operation: (a) LCI input voltage, (b) dc-link current, and (c) electromagnetic torque.

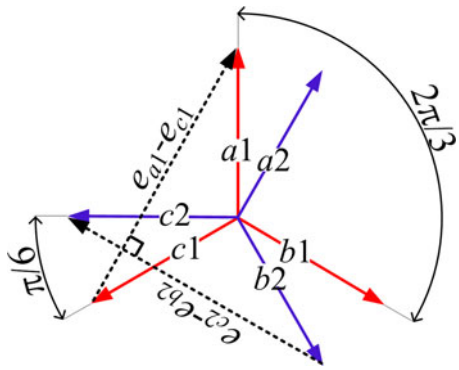

Fig. 25. Phasor diagram of the two three-phase winding sets showing that the magnetic axis of the commutating phases in LCI2, i.e., $e_{c2}(t) - e_{b2}(t)$, is perpendicular to that of the conducting phases in LCI1, i.e., $e_{a1}(t) - e_{c1}(t)$.

for the switching of LCI thyristors, while in the actual system the measured voltages are used for the same purpose. Motor fluxes are less distorted due to the commutation transients than stator voltages and thereby enable a more precise LCI synchronization with the desired firing angle α_m. In addition, all the parasitic effects due to the impedance of the cables connecting the machine and the LCI are present in the measurements but not in the simulations.

VII. Conclusion

LCI-fed WFSM drives are widely used for high-power applications thanks to their established technology, reliability, low cost, and high efficiency. They include various possible topologies, such as the single three-phase one, the dual three-phase arrangement with independent dc links, and the dual three-phase configuration with interconnected dc links. In this paper, a new method has been proposed and experimentally validated to predict the steady-state performance of an LCI drive by computing dc-link current, dc-link voltage, and motor torque waveforms in a fully analytical way. By defining appropriate switching functions, explicit algebraic formulas have been derived covering all the LCI drive configurations of practical interest and enabling the designer to quickly investigate their behavior in a wide variety of operating conditions. Compared to conventional simulation tools based on the numerical solution of differential equations, the proposed method gives almost instantaneous results, requires a very limited knowledge of system parameters and directly yields steady-state current, voltage and torque waveforms with no need to wait for transients to extinguish.

Appendix A

It can be theoretically proved that the commutation transients in one LCI have a negligible distorting effect on the dc-link voltage waveform of the other LCI in a dual three-phase LCI-fed drive. This can be done by writing the voltage-current differential equations of the two three-phase winding sets during each commutation period and showing that the resultant magnetic coupling (mutual inductance) between the commutating phases (belonging to one three-phase winding set) and the conducting phases (belonging to the other three-phase winding set) is negligible. This fact can be also intuitively justified, taking the commutation in LCI2 (see Fig. 1) as an example. The conduction intervals in LCI2 are the same as those shown in Fig. 4 for LCI1 except for a 30 electrical degrees phase shift. For instance, the commutation interval between T6 and T2 (C2 in Fig. 4), starts at $\theta = \theta_{0m} + \pi/3$ while the same commutation interval (let us call it C2$'$), between the same thyristors (let us call them T6$'$ and T2$'$, in LCI2) starts at $\theta = \theta_{0m} + \pi/3 + \pi/6$. Hence, during the interval $\theta_{0m} + \pi/2 < \theta < \theta_{0m} + \pi/2 + \mu_m$, T1 and T2 in LCI1 and T1$'$, T6$'$, and T2$'$ in LCI2 are conducting (assuming that commutations do not overlap in the two LCIs or, in other words $\mu_m < \pi/6$ [10]). In this period, u_{dcm1} is equal to $e_{a1}(t) - e_{c1}(t)$. According to the phasor diagram shown in Fig. 25, the magnetic axis of the commutating phases in LCI2, aligned with the vector $e_{c2}(t) - e_{b2}(t)$, is perpendicular to that of the conducting phases in LCI1, aligned with the vector $e_{a1}(t) - e_{c1}(t)$, indicating the zero mutual coupling in the case of a round rotor. The same can be applied to all the other commutation intervals.

The aforementioned example, i.e., commutation between T6$'$ and T2$'$ in LCI2 and its effect on u_{dcm1}, is also investigated via simulations in Fig. 26. Here, the machine used in Section VI for simulation studies is configured in dual three-phase arrangement

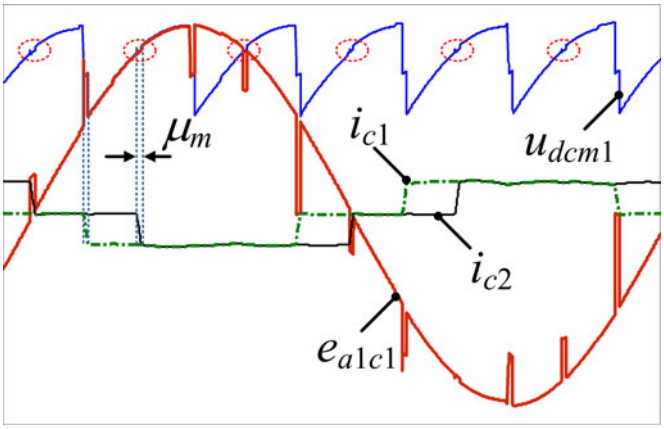

Fig. 26. Simulation waveforms focusing on the effect of commutation between T6′ and T2′ (while i_{c2} changes from 0 to $-I_{\rm dc}$) on $u_{\rm dcm1}$.

with the dc links interconnected. It is evident from Fig. 26 that despite the rotor saliency, the effect of commutation in LCI2 is negligible on $u_{\rm dcm1}$.

Appendix B

As in the case of (4), the equality $\Delta v^L_{y1a1}(t) = -\Delta v^L_{x1a1}(t+\pi/\omega_m)$ can be shown to be true by taking commutation intervals C3 and C6 as examples. According to (15), $\Delta v^L_{x1a1}(t')$ is equal to $-(-e_{a1}(t')+e_{b1}(t'))$ with $(\theta_{0\rm m}+2\pi/3)/\omega_{\rm m} < {\rm t}' < (\theta_{0\rm m}+2\pi/3+\mu_{\rm m})/\omega_{\rm m}$. During C6 (which is displaced by 180 electrical degrees with respect to C3), T5, T6, and T4 are conducting simultaneously and $v_{y1a1}(t'')(t''=t'+\pi/\omega_m)$ is equal to zero because T4 connects phase terminal $a1$ to point $y1$. If the commutation is not taken into account, at interval S6 $(\theta_{0m}+5\pi/3 < \theta < \theta_{0m}+2\pi)$, T6 is conducting and therefore phase terminal $b1$ is connected to point $y1$. Hence, $v^0_{y1a1}(t'')$ is equal to $e_{b1}(t'')-e_{a1}(t'')$ and, consequently, $\Delta v^L_{y1a1}(t'') = v_{y1a1}(t'') - v^0_{y1a1}(t'') = 0-(e_{b1}(t'')-e_{a1}(t''))$. Since the phase back EMFs have sinusoidal waveforms, it can be simply observed that $\Delta v^L_{y1a1}(t) = -\Delta v^L_{x1a1}(t+\pi/\omega_m)$.

Appendix C

The average value of the dc-link current $I_{\rm dc}$ could be calculated according to the motor output power and LCI's input active power such as

$$I_{\rm dc} = \frac{P_m}{N U_{\rm dcm1}\eta}. \tag{C1}$$

Average values $U_{\rm dcm1}$ of $u_{\rm dcm1}$ and $U_{\rm dcg1}$ of $u_{\rm dcg1}$ [see Fig. 1(a)] are

$$U_{\rm dcm1} = \frac{3}{\pi}\sqrt{3}V_m\cos\alpha_m + \frac{3}{\pi}\omega_m L_{Cm} I_{\rm dc} \tag{C2}$$

$$U_{\rm dcg1} = \frac{3}{\pi}\sqrt{3}V_g\cos\alpha_g - \frac{3}{\pi}\omega_g L_{Cg} I_{\rm dc}. \tag{C3}$$

Extracting $U_{\rm dcm1}$ from (C1) and substituting it into (C2), a quadratic equation is obtained where $I_{\rm dc}$ represents the unknown. Among the two solutions of the equation, one is positive and the other is negative. Since thyristor bridges are unidirectional, only the positive solution is kept, which gives

$$I_{\rm dc} = \frac{-\sqrt{3}V_m\cos\alpha_m + \sqrt{3V_m^2\cos^2\alpha_m + (4\pi/3)(P_m/N\eta)\omega_m L_{Cm}}}{2\omega_m L_{Cm}}. \tag{C4}$$

Disregarding the dc-link resistance voltage drop $U_{\rm dcm1} = U_{\rm dcg1}$. Therefore, equalizing (C2) and (C3) and substituting (C4) into them, with some algebraic manipulations (28) is obtained.

Appendix D

The lower integration limit t_0 in (45) is placed in a certain conduction interval $Sj_{m,p}$. Therefore, as illustrated in Fig. 14, it is

$$\left[\theta_{0m} + \frac{\pi}{3}(j_{m,p}-1)\right]\omega_m^{-1} \le t_0 \le \left[\theta_{0m} + \frac{\pi}{3}j_{m,p}\right]\omega_m^{-1}. \tag{D1}$$

From (D1), by few algebraic manipulations, we obtain

$$j_{m,p} \le \frac{3}{\pi}(t_0\omega_m - \theta_{0m}) + 1 \le j_{m,p} + 1. \tag{D2}$$

From this, it is inferred

$$j_{m,p} = \text{trunc}\left[\frac{3}{\pi}(t_0\omega_m - \theta_{0m}) + 1\right]. \tag{D3}$$

We can now prove that $1 \le j_{m,p} \le 6$. In fact, if $1 \le j_{m,p} \le 6$ by (D2), we have

$$1 \le \frac{3}{\pi}(t_0\omega_m - \theta_{0m}) + 1 \le 7. \tag{D4}$$

That is

$$0 \le t_0\omega_m - \theta_{0m} \le 2\pi. \tag{D5}$$

Equation (D5) is true because t_0 has been chosen so that $0 \le t_0/\omega_m - \theta_{0m} \le 2\pi$ (see Fig. 14).

Acknowledgment

The authors would like to thank M. Perna, R. Paletti, and G. Ferrari for their precious support to the experimental validation activities, which have been conducted in the NIDEC-ASI facility in Milan, Italy.

References

[1] A. N. Alcaso and A. J. M. Cardoso, "Remedial operating strategies for a 12-pulse LCI drive system," *IEEE Trans. Ind. Electron.*, vol. 55, no. 5, pp. 2133–2139, May 2008.

[2] J. Song-Manguelle, C. Sihler, and S. Schramm, "A general approach of damping torsional resonance modes in multi-megawatt applications," *IEEE Trans. Ind. Appl.*, vol. 47, no. 3, pp. 1390–1399, May/Jun. 2011.

[3] S. Schramm, C. Sihler, J. Song-Manguelle, and P. Rotondo, "Damping torsional interharmonic effects of large drives," *IEEE Trans. Power Electron.*, vol. 25, no. 4, pp. 1090–1098, Apr. 2010.

[4] B. Wu, J. Pontt, J. Rodríguez, S. Bernet, and S. Kouro, "Current-source converter and cycloconverter topologies for industrial medium-voltage drives," *IEEE Trans. Ind. Electron.*, vol. 55, no. 7, pp. 2786–2797, Jul. 2008.

[5] J. Buckley, "Future trends in commercial and military shipboard power systems," in *Proc. IEEE Power Eng. Soc. Summer Meeting*, Chicago, IL, USA, Jul. 21–25, 2002, pp. 340–343.
[6] S. Castellan, R. Menis, M. Pigani, G. Sulligoi, and A. Tessarolo, "Modeling and simulation of electric propulsion systems for all-electric cruise liners," in *Proc. IEEE Electr. Ship Technol. Symp.*, Arlington, VA, USA, May 21–23, 2007, pp. 60–64.
[7] D. C. Azbill, J. E. Propst, and R. E. Catlett, "A case study of replacing steam turbines with LCI-type variable-speed drives," *IEEE Trans. Ind. Appl.*, vol. 26, no. 6, pp. 1086–1094, Nov./Dec. 1990.
[8] H. Stemmler, "High-power industrial drives," in *Proc. IEEE*, vol. 82, no. 8, pp. 1266–1286, Aug. 1994.
[9] B. Singh, S. Singh, and S. P. H. Chender, "Harmonic mitigation in LCI-fed synchronous motor drives," *IEEE Trans. Energy Convers.*, vol. 25, no. 2, pp. 369–380, Jun. 2010.
[10] A. Tessarolo, S. Castellan, R. Menis, and G. Ferrari, "On the modeling of commutation transients is split-phase synchronous motors supplied by multiple load-commutated inverters," *IEEE Trans. Ind. Electron.*, vol. 57, no. 1, pp. 35–43, Jan. 2010.
[11] A. Tessarolo, C. Bassi, G. Ferrari, D. Giulivo, R. Macuglia, and R. Menis, "Investigation into the high-frequency limits and performance of load commutated inverters for high-speed synchronous motor drives," *IEEE Trans. Ind. Electron.*, vol. 60, no. 6, pp. 2147–2157, Jun. 2013.
[12] K. S. Smith and L. Ran, "Torsional resonance risk management in islanded industrial power systems supplying large VFDs," *IEEE Trans. Ind. Appl.*, vol. 44, no. 6, pp. 1841–1850, Nov./Dec. 2008.
[13] J. Song-Manguelle, S. Schröder, T. Geyer, G. Ekemb, and J.-M. Nyobe-Yome, "Prediction of mechanical shaft failures due to pulsating torques of variable-frequency drives," *IEEE Trans. Ind. Appl.*, vol. 46, no. 5, pp. 1979–1988, Sep./Oct. 2010.
[14] J.-J. Simond, A. Sapin, M. T. Xuan, R. Wetter, and P. Burmeister, "12-pulse LCI synchronous drive for a 20 MW compressor modeling, simulation and measurements," in *Proc. 14th IAS Annu. Meeting*, vol. 4, 2–6, Oct. 2005, pp. 2302–2308.
[15] R. S. Colby, T. A. Lipo, and D. W. Novotny, "A state space analysis of LCI fed synchronous motor drives in the steady state," *IEEE Trans. Ind. Appl.*, vol. IA-21, no. 4, pp. 1016–1022, Jul. 1985.
[16] C.-M. Ong, *Dynamic Simulation of Electric Machinery Using MATLAB/Simulink*. Englewood Cliffs, NJ, USA: Prentice-Hall, 1999.
[17] L. Hu and R. Yacamini, "Harmonic transfer through converters and HVDC links," *IEEE Trans. Power Electron*., vol. 7, no. 3, pp. 514–524, Jul. 1992.
[18] B.-K. Lee and M. Ehsani, "A simplified functional simulation model for three-phase voltage-source inverter using switching function concept," *IEEE Trans. Ind. Electron*., vol. 48, no. 2, pp. 309–321, Apr. 2001.
[19] P. N. Enjeti and P. D. Ziogas, "Analysis of a static power converter under unbalance: A novel approach," *IEEE Trans. Ind. Electron*., vol. 37, no. 1, pp. 91–93, Feb. 1990.
[20] B. K. Bose, *Power Electronics and AC Drives*. Englewood Cliffs, NJ, USA: Prentice-Hall, 1986.
[21] P. A. Hargreaves, B. C. Mecrow, and R. Hall, "Open circuit voltage distortion in salient pole synchronous generators with damper windings," in *Proc. 5th IET Int. Conf. Power Electron., Mach. Drives,* Apr. 2010, pp. 19–21.
[22] R. Krishnan, *Electric Motor drives Modeling, Analysis, and Control*. Englewood Cliffs, NJ, USA: Prentice-Hall, 2001, pp. 36–124.
[23] S. Mohamadian, A. Tessarolo, and A. Shoulaie, "Field oriented control of LCI-fed WFSM drives in stator flux reference frame," in *Proc. 5th Power Electron., Drive Syst. Technol. Conf.,* 5–6, Feb. 2014, pp. 19–24.

Sobhan Mohamadian received the B.Sc. and Ph.D. degrees in electrical engineering from Iran University of Science and Technology (IUST), Tehran, Iran, in 2007 and 2016, respectively.

Between February 2014 and March 2015, he was a Visiting Scholar at the University of Trieste, Trieste, Italy, where he was involved in research projects regarding high-power multiphase motor drives and multiphase machine modeling and analysis. His current research interests include power quality, power electronics, and electrical machines.

Dr. Mohamadian is a Member of Iran's National Elite Foundation (INEF)

Alberto Tessarolo (M'06–SM'15) received the Laurea degree in electrical engineering from the University of Trieste, Trieste, Italy, in 2000, and the Ph.D. degree from the University of Padova, Padova, Italy, in 2011.

Until 2006, he was involved in the design and development of innovative motors and generators for high power applications with NIDEC-ASI (formerly Ansaldo Sistemi Industriali). He is currently with the Department of Engineering and Architecture, University of Trieste, where he is involved in teaching the course of Electric Machine Design. His current research interests include in the area of electric machine and drive modeling, design, and analysis—a field in which he has authored more than 120 scientific papers. He acts as the Principal Investigator for various research projects in cooperation with leading electric machine manufacturers and final users, including the Italian Navy.

Dr. Tessarolo is an Editor for the IEEE TRANSACTIONS ON ENERGY CONVERSION and as an Associate Editor for the IEEE TRANSACTIONS ON INDUSTRY APPLICATIONS and the IET ELECTRIC POWER APPLICATIONS. He is a Registered Professional Engineer in Italy.

Simone Castellan received the Laurea and Ph.D. degrees in electrical engineering from the University of Padova, Padova, Italy.

In 2000, he joined the University of Trieste, Trieste, Italy, as a Researcher dealing with electric power converters, machines, and drives, where he is currently an Assistant Professor of Power Electronics. His current research interests include in the field of power converters for harmonic and flicker compensation, medium-voltage drives, fault-tolerant drives, renewable energy sources, and all-electric ships.

Abbas Shoulaie was born in Isfahan, Iran, in 1949. He received the B.Sc. degree from the Iran University of Science and Technology (IUST), Tehran, Iran, in 1973, and the M.Sc. and Ph.D. degrees in electrical engineering from the Université des Sciences et Techniques du Languedoc (USTL), Montpellier, France, in 1981 and 1984, respectively.

He is currently a Professor of Electrical Engineering at IUST. His current research interests include power electronics, magnetic systems and linear motors, flexible ac current transmission systems (FACTS), and high-voltage dc (HVDC).